Acta Pharmaceutica Sinica B 2026;16(6):3632−3654

Chinese Pharmaceutical Association
Institute of Materia Medica, Chinese Academy of Medical Sciences

Acta Pharmaceutica Sinica B

www.elsevier.com/locate/apsb
www.sciencedirect.com

ORIGINAL ARTICLE

Ginsenoside Rg1 alleviates post-ischemic stroke neuroinflammation by inhibiting CKLF1-mediated suppression of dead/dying neuron clearance

Pinglong Fan[a,b,†], Yuan Ruan[a,†], Kaichao Hu[a], Hongyun Wang[a], Junrui Ye[a], Shasha Wang[c], Ruolan Yuan[a,b], Guangyi Yang[b], Fangmin Liu[b], Wenbin He[d], Gang Li[e], Xu Yan[a], Shifeng Chu[a,*], Zhao Zhang[a,*], Naihong Chen[a,b,c,*]

[a]*State Key Laboratory of Bioactive Substances and Functions of Natural Medicines, Institute of Materia Medica, Chinese Academy of Medical Sciences and Peking Union Medical College, Beijing 100050, China*
[b]*School of Pharmaceutical Sciences, Shenzhen Clinical College of Integrated Chinese and Western Medicine, Guangzhou University of Chinese Medicine, Guangzhou 510000, China*
[c]*Hunan Engineering Technology Center of Standardization and Function of Chinese Herbal Decoction Pieces, College of Pharmacy, Hunan University of Chinese Medicine, Changsha 410208, China*
[d]*National International Joint Research Center for Molecular Chinese Medicine, Shanxi University of Chinese Medicine, Taiyuan 030000, China*
[e]*Graduate School, Inner Mongolia Medical University, Hohhot 010000, China*

Received 6 August 2025; received in revised form 1 December 2025; accepted 1 January 2026

KEY WORDS

Panax notoginseng saponins;
Chemokine-like factor 1;
Target-fishing;
Ginsenoside Rg1;
Ischemic stroke;

Abstract The reduction of dead/dying neurons represents a critical mechanism for the anti-acute ischemic stroke (AIS) effect of *Panax notoginseng*, however, its molecular basis remains unclear. Recent findings implicate chemokine-like factor 1 (CKLF1) as a key contributor to the impaired clearance of dying neurons. Here, we established an integrated high-throughput screening strategy combining biolayer interferometry (BLI), liquid chromatography-tandem mass spectrometry (LC−MS/MS), and NanoBRET technologies to identify CKLF1 inhibitors among *Panax notoginseng* saponins (PNS). Of note, ginsenoside Rg1 (GRg1) exhibits the highest affinity for CKLF1 and the most potent inhibitory efficacy against

*Corresponding authors.
E-mail addresses: chushifeng@imm.ac.cn (Shifeng Chu), zhangzhao@imm.ac.cn (Zhao Zhang), chennh@imm.ac.cn (Naihong Chen).
†These authors made equal contributions to this work.
Peer review under the responsibility of Chinese Pharmaceutical Association and Institute of Materia Medica, Chinese Academy of Medical Sciences.

https://doi.org/10.1016/j.apsb.2026.04.003

Neuroinflammation;
Dead/dying neuron clearance;
Lysosomal dysfunction

the CKLF1−CCR4 interaction, effectively suppressing CKLF1-C27 peptide-induced calcium influx and cytokine production. In experimental AIS models, GRg1 confers neuroprotective properties by mitigating ischemic brain damage and promoting neuronal functional recovery. Mechanistically, GRg1 binds to CKLF1 and modulates the mTORC1/TFEB pathway, enhancing lysosomal function and thereby facilitating the clearance of dead/dying neurons. This study presents an efficient approach for the discovery of natural CKLF1 inhibitors and highlights GRg1 as a promising therapeutic candidate for enhancing the clearance of dead/dying neurons in AIS.

1. Introduction

Acute ischemic stroke (AIS) is a sudden neurologic deficit resulting from focal brain ischemia, ranking as a leading global cause of mortality and disability[1]. The primary pathophysiological mechanisms contributing to cerebral damage following ischemia involve oxidative stress, mitochondrial dysfunction, excitotoxicity, and calcium overload, which collectively trigger extensive neuronal cell death[2,3]. These neurons uncontrollably release damage-associated molecular patterns (DAMP), further exacerbating neuroinflammation and neurological impairments[4]. Microglial clearance of dead/dying neurons is essential for minimizing DAMP release and resolving neuroinflammation during AIS[5,6]. Therefore, enhancing the clearance of dead/dying neurons has emerged as a promising therapeutic strategy for AIS.

Chemokine-like factor 1 (CKLF1), a C−C type chemokine primarily secreted by neurons during AIS, has been implicated in modulating microglial polarization, exacerbating neuroinflammation, and facilitating neutrophil infiltration following ischemic attack[7−9]. Notably, CKLF1 disrupts microglial efferocytosis, resulting in deficient clearance of dying neurons and subsequent accumulation of neuronal debris. The accumulated dead/dying neurons release DAMP, further aggravating neuroinflammatory responses[10]. These findings suggest that therapeutic blockade of CKLF1 may represent an effective strategy to enhance dead/dying neuron clearance following AIS.

Panax notoginseng (Burk.) F. H. Chen, a venerated medicinal plant in Chinese medicine, has been extensively utilized for the management of ischemic conditions. Its bioactive constituent, *Panax notoginseng* saponins (PNS), is approved in China as an adjunctive therapeutic agent for AIS. Preclinical studies[11] have demonstrated that administration of PNS significantly reduces infarct volume and alleviates neurological deficits in AIS models. Proposed neuroprotective mechanisms of PNS include anti-inflammatory effects[12] and reduction of dead/dying neurons[13]. However, whether its ability to reduce dead/dying neurons stems from enhanced clearance, thereby reducing DAMP release and promoting inflammation resolution, remains unclear.

Given that CKLF1 inhibits dead/dying neuron clearance and aggravates neuroinflammation in AIS, while PNS exhibits pharmacological properties of attenuating neuroinflammation and reducing damaged neurons, we hypothesized that PNS may contain natural CKLF1 inhibitors. To validate this speculation, we integrated biolayer interferometry (BLI), ultra-high performance liquid chromatography coupled with a Q Exactive Orbitrap mass spectrometer in tandem mass spectrometry mode (UHPLC−Q Exactive Orbitrap-MS/MS), and NanoBRET assays. Results revealed that GRg1, a key candidate compound, exhibited the highest affinity to CKLF1 and potently inhibited CKLF1−CCR4 interactions. Moreover, GRg1 was shown to alleviate ischemic injury by accelerating dead/dying neuron clearance. Mechanistically, GRg1 targets CKLF1 and promotes microglial degradation *via* modulation of the mTORC1/TFEB signaling cascade. This study establishes an efficient CKLF1-targeted screening strategy for ischemic stroke therapy and highlights GRg1 as a promising therapeutic candidate for the clearance of dead/dying neurons in AIS.

2. Materials and methods

2.1. Cell culture

HEK-293T cells (CL-0005), BV-2 microglia (CL-0493), and SH-SY5Y neuroblastoma cells (CL-0208) were purchased from Procell (Wuhan, China) and cultured in Dulbecco's modified Eagle's medium (DMEM) supplemented with 10% fetal bovine serum (FBS) and 50 U/mL penicillin−streptomycin. The cultures were maintained in a humidified incubator with 5% CO_2 at 37 °C. The SH-SY5Y-mCherry cells were created *via* stable transfection of the SH-SY5Y cell line with the mCherry red fluorophore (OBiO Technology) for conducting apoptotic cell (AC) degradation assays.

2.2. Experimental animals

The animal protocols employed in this study were approved by the Institutional Animal Care and Use Committee of Peking Union Medical College and the Chinese Academy of Medical Sciences (Approval No. IMM-N-25-0054). Mice were socially housed under a 12-h light−dark cycle, with *ad libitum* access to water and food. All subjects were of the C57BL/6J genetic background. C57BL/6J mice were procured from Charles River Laboratories (Beijing, China), while *Cklf1*$^{-/-}$ mice were generously provided by Dr. Lianfeng Zhang from Peking Union Medical College (Beijing, China). Male mice, aged 8 to 10 weeks, were utilized in this investigation, and all mice were randomly assigned to their respective experimental groups.

2.3. Reagent or resource

Comprehensive details regarding the reagents or resources employed are provided in Supporting Information Table S1.

2.4. BLI analysis

Ni-NTA biosensors (FortéBio) were initially pre-wetted with PBS to establish a baseline. Subsequently, the biosensors were coated with His-tagged CKLF1 at a concentration of 50 μg/mL within 96-well black F-bottom plates (Greiner Bio-One, Frickenhausen, Germany). Various concentrations of PNS solution (62.5−1000 μg/mL), diluted in ultrapure water containing 5% DMSO and 0.02% Tween 20, were added to the 96-well black F-bottom plates at a volume of 200 μL per well. Concurrently, a control well was set using the same vehicle. A total of four critical steps, including loading for 300 s, baseline for 60 s, association for 30 s, and dissociation for 30 s, were repeated in cycles. Data acquisition and analysis were performed using FortéBio Octet Analysis software (Sartorius AG, Goettingen, Germany).

2.5. UHPLC−Q Exactive Orbitrap-MS/MS identification

Samples of PNS solution used for the BLI assay and the dissociation buffer with or without PNS were lyophilized and dissolved in HPLC-grade methanol, vortexed, and centrifuged at 13,400 × *g* for 10 min at 4 °C. The resulting supernatant was filtered through a 0.22 μm filter and transferred into disposable glass auto-sampler vials. Liquid chromatographic separation was conducted using a Thermo Scientific UltiMate 3000 RS system (Thermo Scientific, CA, USA) equipped with an AQ-C18 column (1.8 μm, i.d. 2.1 mm × 150 mm; Welch Materials, Inc.) and coupled to a Thermo Scientific Q Exactive mass spectrometer (Thermo Scientific). The mobile-phase solvents consisted of 1% formic acid (A) and methanol (B). Gradient elution was employed using the following conditions: column temperature of 35 °C, injection volume of 5 μL, and flow rate of 0.3 mL/min. The elution program was set as follows: 0−1 min, 2% B; 1−5 min, 2%−20% B; 5−10 min, 20%−50% B; 10−15 min, 50%−80% B; 15−20 min, 80%−95% B. Data acquisition and processing were performed using CD 3.3 software (Thermo Fisher Scientific).

2.6. NanoBRET assay

HEK293T cells at a concentration of 2×10^5 cells/mL were seeded into poly-L-ornithine-coated 96-well plates and incubated overnight for transient transfections. The following day, transfection mixes containing a 1:1 ratio of HaloTag-CKLF1 to NanoLuc-CCR4 constructs with a total concentration of 100 ng per well, and 0.3 μL of ViaFect™ transfection reagent (Promega) per well in OptiMEM (Gibco), were prepared. These mixtures were incubated for 10 min before being added to the plate at 5 μL per well. The cells were then incubated overnight to allow expression.

The medium was removed from 96-well microplates containing transfected cells and replaced with either 50 μL HBSS containing 1 μL of 0.1 mmol/L HaloTag® NanoBRET™ 618 ligand or a control vehicle. The plate was incubated for 4 h, and NanoBRET™ Nano-Glo® Substrate was added for BRET signal measurement using a PerkinElmer Envision 2104 Plate Reader (PerkinElmer, MA, USA) with 460 and 615 nm filters. CKLF1−CCR4 binding assays were normalized to a final DMSO concentration of 0.1%. The raw NanoBRET ratio was calculated by dividing the emission at 615 nm by that at 460 nm, and the resultant values were subjected to non-linear regression analysis using GraphPad Prism 9.5 (GraphPad Software, CA, USA).

2.7. Microscale thermophoresis (MST)

CKLF1 was labeled using the RED-NHS kit (NanoTemper Technologies, Munich, Germany) according to the manufacturer's instructions. The binding affinity between GRg1 and CKLF1 was determined using a Monolith NT.115 instrument (NanoTemper Technologies, Munich, Germany).

2.8. Intracellular calcium ion concentration detection

The human pcDI-CCR4 and empty pcDI vectors were transfected into HEK-293 cells using Lipofectamine™ 2000 (Invitrogen, CA, USA) in accordance with the manufacturer's protocol. To maintain stable CCR4 expression, the transfected HEK-293 cells were subsequently treated with geneticin (G418) at a final concentration of 500 μg/mL 48 h post-transfection. Monoclonal cell lines of stably transfected cells were then selected and expanded. The expression of CCR4 was confirmed by Western blotting.

HEK293-CCR4 (CCR4-overexpressing) and HEK293-NC cells were loaded with the fluorescent calcium indicator Fluo-4 AM (Yeasen, Shanghai, China) according to the manufacturer's instructions. Real-time fluorescence images were acquired using a confocal microscope (Cytation 10; Agilent BioTek, CA, USA) prior to and following stimulation with CKLF1-C27 and/or GRg1, with images captured at 2-s intervals.

2.9. Oxygen-glucose deprivation/reoxygenation

Aspirate the regular culture medium and gently wash cells twice with PBS to remove residual glucose and serum. Replace with glucose-free DMEM (without FBS) to establish the glucose deprivation condition. Transfer the cell culture plates to a hypoxic chamber infused with 95% N_2 and 5% CO_2. Incubate cells under hypoxic and glucose-free conditions at 37 °C for 2 h.

After the OGD period, carefully remove the glucose-free DMEM and wash the cells once with PBS to eliminate the hypoxic medium. Replace it with regular complete DMEM containing 10% FBS and glucose to restore nutrient supply. Return the cells to a normoxic incubator (5% CO_2, 37 °C) for a 24-h reoxygenation period prior to further analysis.

2.10. Isolation of primary microglia and neurons

Primary microglia and neurons were isolated from the brains of newborn WT or *Cklf1*$^{-/-}$ mice. In brief, after removing blood vessels and meninges, the brain tissues were minced and digested with 0.25% trypsin-EDTA for 15 min. The digested tissues were then centrifuged at 1000 rpm for 6 min, and microglia or neurons were subsequently isolated using different media. For primary microglia, the mixture of cells was inoculated into poly-D-lysine-coated T25 flasks and cultured in DMEM/F12 supplemented with FBS, penicillin, and streptomycin. After 14 days of *in vitro* culture, the flasks were shaken at 200 rpm and 37 °C for 6 h to harvest mature microglia. The supernatant containing microglia was collected for further experiments. For primary neurons, the cells were seeded on poly-D-lysine pretreated plates and incubated in Neurobasal™ medium containing 2% B27 supplement, penicillin, and streptomycin. Neurons were collected after 7 days of *in vitro* culture.

2.11. Gene expression analysis

Total RNA was extracted using TRIzol reagent and reverse-transcribed with the TransScript® One-Step gDNA Removal and cDNA Synthesis SuperMix kit, following the manufacturer's instructions. Quantitative PCR (qPCR) was conducted on a 7500 Real-time PCR system (Applied Biosystems, CA, USA) using the PerfectStart® Green qPCR SuperMix Kit. The sequences of the primers used are detailed in Supporting Information Table S2.

2.12. Transient middle cerebral occlusion (tMCAO) in murine models

Transient cerebral ischemia was induced by intraluminal occlusion of the left middle cerebral artery (MCA) for a duration of 90 min, as previously described[14]. Sham-operated animals received identical anesthetic protocols and arterial exposure without MCA occlusion. Specifically, male C57BL/6J mice, including both wild-type (WT) and *Cklf1*$^{-/-}$ strains, aged 8 to 10 weeks and weighing between 21 and 25 g, were anesthetized with a mixture of 2% isoflurane in oxygen for induction, followed by maintenance with 1.5% isoflurane. The tMCAO model was established by introducing a silicone-coated monofilament (RWD Life Science, Shenzhen, China) into the MCA *via* the internal carotid artery, which was left in position for 90 min to effectively reduce MCA blood flow. A rectal temperature of 37.0 ± 0.5 °C was meticulously regulated using a temperature-controlled heating pad throughout the surgical procedure. The adequacy of ischemia was verified using a laser speckle imaging system (RWD Life Science). Mice demonstrating less than a 30% reduction in baseline blood flow during the occlusion were excluded from the study.

2.13. Intracerebroventricular injection

WT or *Cklf1*$^{-/-}$ mice were anesthetized with isoflurane and injected with 10 μg of CKLF1 or CKLF1-C19 dissolved in PBS *via* intracerebroventricular (ICV) injection into the right lateral ventricle at the designated time points, respectively. The stereotactic injection coordinates were 0.5 mm anterior-posterior, 1.0 mm right medial-lateral, and −2.3 mm dorsal-ventral relative to the bregma.

2.14. Animal grouping and administration

Male C57BL/6J WT mice, *Cklf1*$^{-/-}$ mice, and CKLF1-rescue mice (generated by intracerebroventricular injection of recombinant CKLF1 into *Cklf1*$^{-/-}$ mice) were used, aged 8−10 weeks and weighing 21−25 g.

Pharmacodynamic evaluation of GRg1 in the treatment of ischemic stroke: Mice were randomly assigned to the following groups: Sham group (underwent identical anesthetic and surgical procedures without tMCAO); Model group (underwent tMCAO and vehicle *via* intragastric administration (i.g.) or intracerebroventricular injection); GRg1 treatment groups (administered GRg1 at doses of 10, 20, or 40 mg/kg *via* i.g.); and positive control groups, including the PNS group (administered PNS at 100 mg/kg *via* i.g.), NBP group (administered *n*-butylphthalide at 80 mg/kg *via* i.g.), and CKLF1-C19 group (administered the CKLF1 antagonist peptide CKLF1-C19 at 10 μg *via* ICV). Regarding the timing and frequency of administration: GRg1, PNS, and NBP were first administered during the tMCAO occlusion phase, with additional doses administered at 24 and 48 h post-surgery; CKLF1-C19 was administered as a single ICV during the tMCAO occlusion phase. For the assessment of brain functional connectivity, mice in the GRg1 group were continuously administered GRg1 (40 mg/kg) for 7 days (initiated during the occlusion phase and maintained daily for 7 days post-surgery) to evaluate its long-term restorative effects on brain networks.

Experimental protocol for GRg1 exerting anti-ischemic effects by targeting CKLF1: WT mice, *Cklf1*$^{-/-}$ mice, and CKLF1-rescue mice were utilized to establish the tMCAO model. Each mouse strain was randomly assigned to two groups ($n = 6$ per group) and received GRg1 (40 mg/kg) or vehicle *via* i.g. during the occlusion phase, as well as at 24 and 48 h post-occlusion.

2.15. Laser speckle imaging

A laser speckle imaging system (RWD Life Science) was used for real-time cerebral blood flow (CBF) monitoring. The system was calibrated according to the manufacturer's instructions before each experiment to ensure consistent light intensity and imaging parameters. Mice were placed in a prone position on a heated platform. The scalp was carefully shaved and cleansed, and a rostrocaudal incision was made to expose the underlying skull. The laser speckle imaging probe was positioned perpendicular to the mouse skull, centered over the cerebral cortex (covering both ipsilateral and contralateral hemispheres relative to the ischemic site) at a fixed distance to ensure uniform imaging field coverage. Before tMCAO induction, baseline CBF was recorded. During the 90-min MCA occlusion period, laser speckle imaging was performed to verify the adequacy of ischemia. After filament withdrawal, CBF was monitored immediately. For the intervention groups, additional imaging was conducted 2 h after the final drug administration.

2.16. MRI scans

Mice were anesthetized with 2% isoflurane for induction and maintained at 1.5% isoflurane throughout the imaging acquisitions. Experiments were conducted on a Pharmascan 70/16 MRI system, with data acquired using Paravision 6.0.1 software (Bruker, Carlsruhe, Germany). T2-weighted images were obtained using a multislice multiecho sequence (echo time/repetition time (TE/TR: 15 ms/2000 ms). Structural MRI and functional MRI were performed on Days 2 and 7 post-tMCAO, respectively. The methodologies for assessing brain structural damage and evaluating functional connectivity have been detailed in our previous studies[15,16].

2.17. Neurological deficit evaluation and behavioral assessments

Neurological deficit evaluation: Neurological deficits in mice were assessed using the modified neurological severity score (mNSS), as previously described[17,18]. This scoring system encompasses evaluations of motor abilities, reflex responses, and balance, with total scores reflecting the severity of neurological impairment ranging from 0 (indicating no observable symptoms) to 18 (most severe deficits). mNSS assessments were performed 2 days post-operatively.

Behavioral assessments: Behavioral analyses, including grip strength, grid walking, corner turning, and rotarod tests, were performed 2 days post-operatively, as previously described in detail[19,20].

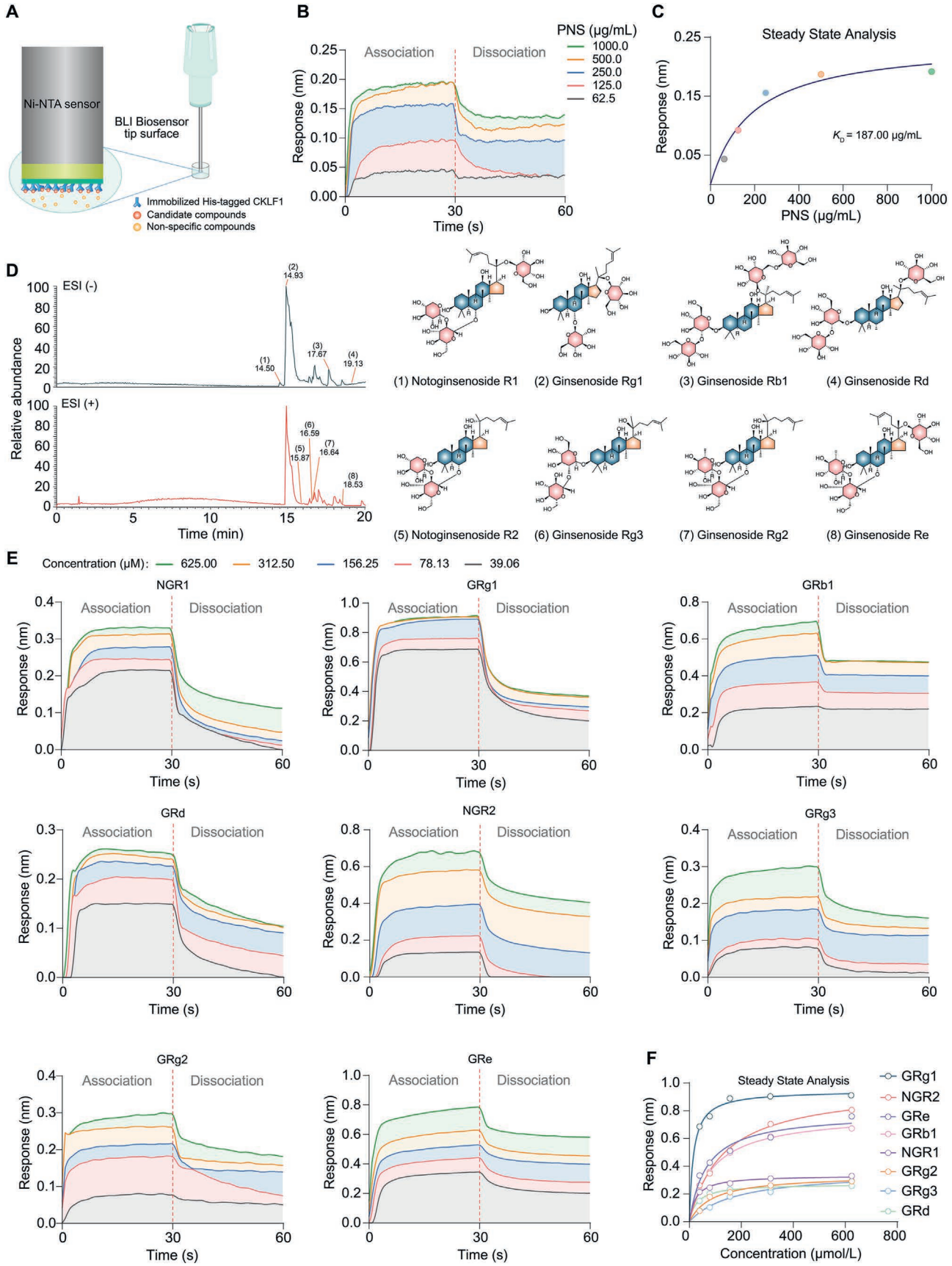

Figure 1 Screening and identification of CKLF1 binders in PNS. (A) Schematic diagram for target-fishing of CKLF1-binding natural small molecules from PNS. (B) Real-time kinetic binding sensorgrams of different concentrations of PNS (62.5 to 1000 μg/mL) are shown. Response

2.18. HE and nissl staining

HE and Nissl staining were used to assess histopathological damage as previously described[16]. For HE staining: In the peri-infarct region of mouse brain sections, damaged neurons (identified by cytoplasmic shrinkage and hyperchromatic condensation) were counted in 3 randomly selected microscopic fields per section by two independent blinded observers. For Nissl staining: Viable neurons (characterized by intact, large soma with distinct Nissl bodies) were quantified in the same peri-infarct regions and using the same counting method as for HE staining.

2.19. Brain distribution of GRg1 and its metabolites in the tMCAO model

Male C57BL/6J mice were subjected to tMCAO or sham operation. GRg1 (100 mg/kg) was intragastrically administered during the occlusion phase. At 1, 2, 3, 4, 6, 8, 12, and 24 h post-GRg1 administration, mice were euthanized, and brain tissues were harvested, including the ipsilateral (Ci) and contralateral (Cii) hemispheres to the infarction (for tMCAO mice) and corresponding regions (Ciii) for sham mice. Brain samples were lyophilized, dissolved in HPLC-grade methanol, centrifuged (13,400 × *g*, 10 min, 4 °C), filtered (0.22 μm), and analyzed *via* LC−MS/MS to quantify GRg1 and its metabolites (GRh1, GF1, 20(*S*)-protopanaxatriol). Pharmacokinetics data analysis, including parameters such as C_{max} (maximum observed concentration), T_{max} (time of C_{max}), and AUC_{0-last} (area under the curve from the time of dosing to the last measurable concentration), was conducted using the non-compartmental model in WinNonlin Version 8.2 statistical software (Pharsight Corporation, CA, USA).

2.20. HMGB1 and HSP70 ELISAs

To assess HMGB1 and HSP70 levels in peri-infarct tissues of WT mice post-tMCAO, tissues were harvested after transcardial perfusion with PBS and lysed in RIPA buffer supplemented with a cocktail of protease and phosphatase inhibitors. The resulting samples were analyzed in duplicate using commercially available ELISA kits, according to the manufacturer's protocols.

2.21. Immunofluorescence microscopy

Coronal brain sections and cell coverslips underwent immunofluorescence staining, according to established protocols[21]. Briefly, free-floating brain sections were blocked with 5% bovine serum albumin in 0.5% Triton X-100/PBS for 1 h at 25 °C. Subsequently, they were incubated with primary antibodies overnight at 4 °C. Following three washes with 0.1% PBST, the sections were incubated with appropriate secondary antibodies and Hoechst stain for 1 h at room temperature. The immunofluorescence protocol employed for the cell coverslips mirrored that for coronal brain sections, with minor adjustments to reagent concentrations: BSA was used at a concentration of 3%, while Triton X-100 in PBS was adjusted to 0.2%. After thorough washing, the sections were mounted with Fluoromount-G. All secondary antibodies were diluted at a ratio of 1:500. Image acquisition was carried out using a confocal microscope (Cytation 10; Agilent BioTek, CA, USA). One or two randomly selected microscopic fields within the peri-infarct regions of the external capsule, cortex, and striatum were analyzed per section. Image analysis was performed in ImageJ software (NIH, MD, USA) by two independent, blinded observers. Positively stained cells were electronically labeled to prevent duplicate counting. The infarct area was identified by shrunken Hoechst-stained nuclei, whereas the infarct border was characterized by the absence of fluorescence staining and the accumulation of $Iba1^+$ microglia. The peri-infarct region was delineated as tissue located within a radial distance of 200−300 μm from the infarct border.

2.22. Immunoblot assay

The collected brain tissues were lysed in RIPA buffer supplemented with a protease inhibitor and a phosphatase inhibitor cocktail. Protein concentrations were determined using a BCA Protein Assay Kit. Equal quantities of protein were subjected to SDS-PAGE and subsequently transferred to polyvinylidene difluoride membranes. Following a 1-h blocking step with 5% BSA at room temperature, the membranes were incubated with primary antibodies overnight at 4 °C. This was followed by incubation with appropriate HRP-conjugated secondary antibodies for 1 h at room temperature, and protein detection was achieved using enhanced chemiluminescence substrate. Images were captured with an Image Quant LAS 4000 mini (GE Healthcare, WI, USA) and analyzed using ImageJ software (NIH, MD, USA).

2.23. Apoptosis induction

SH-SY5Y or SH-SY5Y-mCherry cells were treated with 3 μmol/L staurosporine for 4 h to induce apoptosis[22]. The cells were gently washed twice with PBS and harvested in DMEM supplemented with 10% FBS for further experimental analyses.

2.24. CRISPR/Cas9 knockout target genes in BV2 microglia

To achieve knockout of the *Ccr4* and *Tfeb* genes in BV-2 microglia, we utilized the ChOPChOP single-guide RNA (sgRNA) design system to construct sgRNAs and cloned the corresponding target sequences into the lentiCRISPRv2 vector (Addgene, MA, USA). Lentivirus carrying the sgRNAs specific to the target genes, as well as a vector control, were generated in HEK-293T cells using standard lentiviral packaging protocols. Following infection of BV-2 microglia with the lentivirus for 48 h, we selected for genetically modified cells using puromycin (2 μg/mL) for 10 days and obtained the target

(nm) indicates the optical thickness on the Ni-NTA biosensor layer. (C) Equilibrium binding signal was achieved, as revealed by the flattened curve. (D) The total ion chromatogram (TIC) and component characterization of the dissociation buffer containing PNS, as recorded by UHPLC−Q Exactive Orbitrap-MS/MS. (E) Real-time kinetic binding sensorgrams of the identified binding components with CKLF1. (F) Equilibrium binding parameters of CKLF1 with BLI-fished candidates: GRg1: K_D = 15.52 μmol/L, B_{max} = 0.95 nm; NGR2: K_D = 225.10 μmol/L, B_{max} = 0.94 nm; GRe: K_D = 66.25 μmol/L, B_{max} = 0.78 nm; GRb1: K_D = 91.26 μmol/L, B_{max} = 0.78 nm; NGR1: K_D = 25.00 μmol/L, B_{max} = 0.33 nm; GRg2: K_D = 90.18 μmol/L, B_{max} = 0.34 nm; GRg3: K_D = 177.30 μmol/L, B_{max} = 0.37 nm; GRd: K_D = 29.69 μmol/L, B_{max} = 0.27 nm. μM: μmol/L.

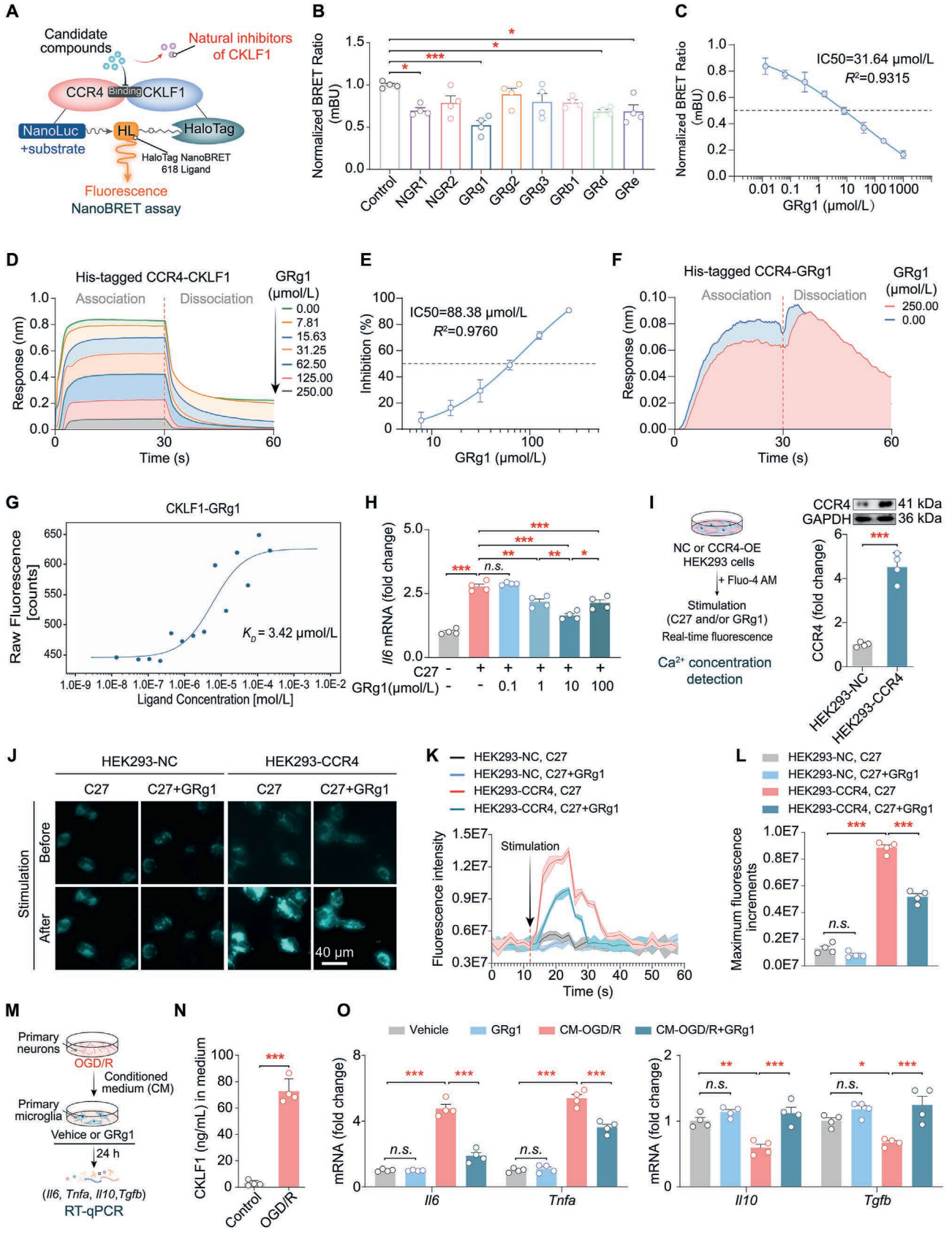

Figure 2 Screening and validation of candidate compounds for their bioactivity against CKLF1. (A) A NanoBRET-based screening approach for identifying inhibitors targeting the CKLF1−CCR4 interaction in live cells. HEK293T cells were co-transfected with NanoLuc-tagged CCR4 and HaloTag-conjugated CKLF1 expression vectors, followed by the addition of BRET ligand and substrate to the cells. If the two proteins were

monoclonal stable cell lines. Knockout of target genes in individual monoclonal cell lines was confirmed *via* Western blot analysis.

2.25. Phagosomal cargo degradation

BV-2 cells were co-cultured with apoptotic SH-SY5Y-mCherry cells for 3 h, after which the cultures were meticulously washed. Confocal microscopy was employed to capture images immediately (designated as time 0), followed by additional incubation for 3 or 6 h prior to re-imaging to assess cargo degradation.

2.26. Lysosomal acidification and lyso-tracker staining

BV-2 cells (5×10^4 cells/well) were plated in a 24-well plate and then co-incubated with apoptotic SH-SY5Y cells in the presence of GRg1 and/or CKLF1-C27 at 37 °C for 3 h. Following incubation, the cells were washed twice with PBS to remove any non-engulfed apoptotic cells. BV-2 cells were then incubated for an additional 3 h. Medium containing 1 μmol/L LysoSensor (for lysosomal acidification assay) or 50 nmol/L LysoTracker was added for a further 30-min incubation at 37 °C. Confocal images were acquired using a Cytation 10 microscope (Agilent BioTek, CA, USA) for fluorescence observation, with at least three images captured per well for both the lysosomal acidification and Lysotracker staining assays. For lysosomal acidification analysis, the fluorescence intensity of LysoSensor staining was quantified per unit area (4 random fields per group) and in 20 individual cells per group. For lysosomal morphology (LysoTracker staining) analysis: In BV-2 microglia, the mean diameter and Maximum diameter of lysosomes in 10 randomly selected cells per group were quantified by Image J software.

2.27. LGALS3-puncta and TFEB nuclear translocation

Cellular treatment protocol was performed as described in the lysosomal acidification and LysoTracker staining assays. After removing non-engulfed ACs and incubating for 3 h, BV-2 cells were fixed with 4% paraformaldehyde for 15 min at room temperature. LAMP1 (a lysosomal marker) and LGALS3 antibodies were used for the LGALS3 puncta assay, while TFEB antibody and Hoechst 33342 (a nuclear marker) were used to assess TFEB nuclear translocation. The percentage of $LGALS3^+LAMP1^+$ cells was counted in four random fields per group. For TFEB nuclear translocation analysis in BV-2 microglia, four random microscopic fields per group were captured *via* confocal microscopy. Cells with TFEB predominantly localized to the nucleus (colocalized with Hoechst 33342) were counted by two independent blinded observers. The percentage of TFEB nuclear-positive cells relative to the total number of cells was calculated.

2.28. Transwell migration assay

Approximately 5×10^4 BV-2 microglia were cultured in serum-free DMEM with or without cytochalasin D (Cyto D), and seeded into the upper chamber of fibronectin-precoated Transwell plates (8 μm pore size, Costar, Sigma−Aldrich #3464). ACs treated with CKLF1-C27 and/or GRg1 were placed in the lower chamber, which was supplemented with DMEM containing 10% FBS to induce chemotaxis. After 24 h of Transwell migration, crystal violet-stained migrated cells on the bottom surface of the upper chamber were counted in four random microscopic fields per group by two blinded observers.

2.29. CCK-8 assay

Primary neurons isolated from *Cklf1*$^{-/-}$ mice were seeded in a 96-well plate and subjected to OGD/R. During reperfusion, neurons were treated with CKLF1-C27 (1 μmol/L), CCL17 (1 μmol/L), and/or GRg1 (10 μmol/L) for 24 h. After treatment, cell viability was detected strictly according to the CCK-8 kit manufacturer's instructions.

within 10 nm of each other, BRET fluorescence was detected. (B) Normalized BRET ratio of HEK293 cells in the presence of candidate compounds (10 μmol/L) ($n = 4$; $^{*}P < 0.05$, $^{***}P < 0.001$, one-way ANOVA followed by Tukey's *post hoc* test). (C) GRg1 dose-dependently reduced the NanoBRET signal for CKLF1−CCR4 binding with an IC_{50} of 31.64 μmol/L (D, E) GRg1 interferes with the binding of CKLF1 to CCR4. A BLI system equipped with Ni-NTA biosensors was used to monitor the association/dissociation of His-tagged CCR4 (50 μg/mL) with CKLF1 (50 μg/mL) in the presence or absence of GRg1. A series of GRg1 concentrations (7.81, 15.63, 31.25, 62.50, 125.00, and 250.00 μmol/L) was selected to determine the IC_{50} value. (F) A BLI system equipped with Ni-NTA biosensors was used to monitor the association/dissociation of His-tagged CCR4 (50 μg/mL) with GRg1 (250 μmol/L). (G) Direct binding of CKLF1 to GRg1 was investigated by MST. Changes in the thermophoretic signal of the CKLF1−GRg1 complex yielded a K_D of 3.42 μmol/L. (H) To investigate the effect of GRg1 on CKLF1-C27-induced elevation of *Il6* mRNA expression, BV-2 microglia were incubated with 0.1−100 μmol/L GRg1 and/or 1 μmol/L CKLF1-C27, followed by qPCR analysis ($n = 4$; $^{*}P < 0.05$, $^{**}P < 0.01$, $^{***}P < 0.001$, one-way ANOVA followed by Tukey's *post hoc* test). (I) Calcium flux was assessed in HEK293-CCR4 and HEK293-NC cells following stimulation with CKLF1-C27 (1 μmol/L) and/or GRg1 (10 μmol/L). HEK293-CCR4 cells exhibited higher CCR4 expression compared with HEK293-NC cells ($n = 4$; $^{***}P < 0.001$; two-tailed Student's *t* test). (J) Representative fluorescence images of HEK293-CCR4 and HEK293-NC cells pre- and post-stimulation with CKLF1-C27 and/or GRg1, loaded with Fluo-4 AM, are presented. (K) The temporal alterations in fluorescence intensity associated with calcium flux were quantified over a 60-s period ($n = 4$). (L) Maximum fluorescence increments observed following stimulation with CKLF1-C27 and/or GRg1 in HEK293-CCR4 and HEK293-NC cells ($n = 4$; $^{***}P < 0.001$, n.s.: non-significant; two-way ANOVA followed by Sidak's multiple comparison test). (M) Experimental design to investigate the efficacy of GRg1 intervention in mitigating primary microglial inflammation induced by conditioned medium (CM) from OGD/R-stimulated primary neurons. Specifically, primary neurons were subjected to 2 h of OGD followed by reoxygenation to prepare the conditioned medium. Primary microglia were then exposed to CM from OGD/R-stimulated primary neurons, followed by treatment with vehicle or GRg1 (10 μmol/L) for 24 h. Subsequent analyses included: (N) Quantification of CKLF1 concentration in the conditioned medium *via* ELISA ($n = 4$; $^{***}P < 0.001$; two-tailed Student's *t*-test); (O) Evaluation of microglial inflammatory responses using qPCR ($n = 4$; $^{*}P < 0.05$, $^{**}P < 0.01$, $^{***}P < 0.001$, one-way ANOVA followed by Tukey's *post hoc* test). All data are presented as mean±SEM.

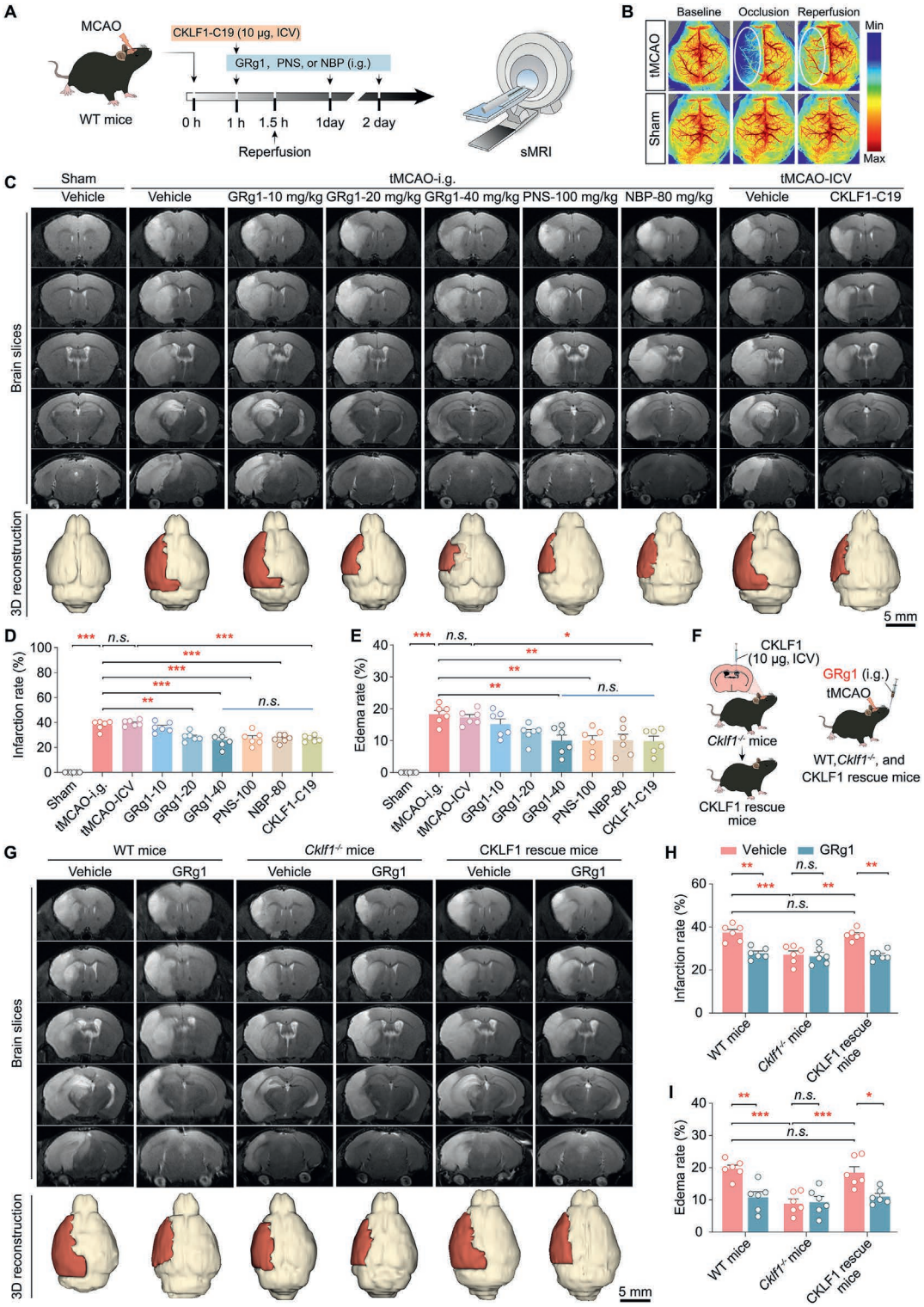

Figure 3 GRg1 alleviates cerebral damage post-ischemia in a CKLF1-dependent manner. (A) Schematic representation of the experimental protocol. C57BL/6J mice underwent tMCAO, with reperfusion initiated 1.5 h post-occlusion. GRg1 (10−40 mg/kg), PNS (100 mg/kg), and NBP (80 mg/kg) were administered intragastrically during the occlusion phase, as well as at 24 and 48 h post-tMCAO; CKLF1-C19 (10 μg) was administered *via* intracerebroventricular injection as a single dose during the occlusion phase. Two hours after the final dose, sMRI, behavioral assessments, and histopathological evaluations (HE and Nissl staining) were performed. (B) Representative images of cerebral blood flow monitored by laser speckle imaging. (C) Representative images of brain slice morphology and 3D reconstructions derived from sMRI data using 3D Slicer software (Kitware, Inc., NY, USA). (D, E) Cerebral infarction rate and edema rate ($n = 6$; $^{*}P < 0.05$, $^{**}P < 0.01$, $^{***}P < 0.001$; one-

2.30. Quantification and statistical analysis

The normality of the data was assessed using the Shapiro-Wilk test, and statistical significance was evaluated using SPSS 29.0 software (IBM, NY, USA). Data that met the criteria for normality were analyzed using two-tailed Student's *t*-test for comparisons between two groups with a single variable and equal variances, one-way ANOVA followed by Tukey's *post hoc* test for multiple groups involving a single variable, or two-way ANOVA with Sidak's multiple comparison test for comparisons among more than two groups involving multiple variables. For non-normally distributed data with equal variances, the nonparametric Mann−Whitney U test was used. All displayed are one representative experiment from at least three independent repetitions and presented as the mean±standard error of mean (SEM). Differences were considered statistically significant at $P < 0.05$. Data were post-processed using Excel 2021 (Microsoft, WA, USA), Prism 9.5 (GraphPad, CA, USA), and Illustrator 2020 (Adobe, CA, USA). Brain slice morphology and 3D reconstructions were derived from sMRI data using 3D Slicer software (Kitware, Inc., NY, USA). 3D surface rendering and pseudo-coloring were performed with Imaris 9.0.1 (Bitplane, Zurich, Switzerland).

3. Results

3.1. GRg1 exhibits the highest affinity for CKLF1 among PNS

To determine whether PNS interacts with CKLF1, we employed a BLI analysis system equipped with Ni-NTA sensors to assess the affinity between PNS and CKLF1 across a concentration gradient (62.5−1000 μg/mL) (Fig. 1A). Our findings revealed a direct and reversible binding between PNS and CKLF1 (K_D = 187.00 μg/mL), as evidenced by a concentration-dependent increase in optical thickness (nm) on the Ni-NTA sensor layer with increasing PNS concentrations (62.5 to 500 μg/mL) (Fig. 1B and C). Based on these observations, a PNS concentration of 500 μg/mL was selected for the subsequent experiments.

To identify small molecules within the PNS−CKLF1 complex, we collected dissociation buffers with or without PNS from biosensor assays over 30 cycles. In parallel, an equal volume of the PNS solution (500 μg/mL) used in the BLI assay was prepared as a positive control. UHPLC-Q Exactive Orbitrap-MS/MS analysis of these samples identified eight components in the CKLF1−PNS dissociation buffer (Supporting Information Fig. S1), based on LC−MS/MS data (retention time, MS^n multi-level fragments, molecular weight), total ion chromatography, and the MzCloud database[23−25]. These compounds consist of five triol-type ginsenosides (notoginsenoside R1 (NGR1), NGR2, GRg1, GRg2, and GRe) and three diol-type ginsenosides (GRb1, GRd, and GRg3) (Fig. 1D and Fig. S1). To identify the ginsenoside with the optimal CKLF1 binding affinity within the CKLF1−PNS complex, we performed BLI to assess the binding affinities of the eight ginsenosides. Of the eight candidates tested, GRg1 exhibited the strongest affinity with a K_D of 15.52 μmol/L and a maximum binding capacity (Bmax) of 0.95 nm (Fig. 1E and F).

3.2. GRg1 blocks CKLF1/C27-mediated biological effects

To explore the pharmacological properties of candidate compounds on CKLF1 bioactivity, we developed a NanoBRET-based screening assay to quantify the CKLF1−CCR4 interaction, which is known as a key protein−protein interaction mediating CKLF1 function in microglia[26]. Our results showed that NGR1, GRg1, GRd, and GRe effectively impeded CKLF1−CCR4 binding in HEK-293T cells at 10 μmol/L, with GRg1 exhibiting the highest inhibitory effect (52.55%). Subsequent kinetic analysis further demonstrated that GRg1 blocked the CKLF1−CCR4 interaction in a concentration-dependent manner (0.013−1000.0 μmol/L), achieving a maximal inhibition of 83.51% and an IC_{50} of 31.64 μmol/L (Fig. 2A−C), highlighting the potent efficacy of GRg1 in disrupting the CKLF1−CCR4 complex. To further investigate the effect of GRg1 on the interaction kinetics of CKLF1 and CCR4, we employed BLI equipped with Ni-NTA biosensors to detect the association and dissociation process of His-tagged CCR4 and CKLF1 in the presence or absence of GRg1. Our data revealed that GRg1 significantly reduced the binding affinity between CKLF1 and CCR4. Specifically, GRg1 inhibited CKLF1 binding to CCR4 with an IC_{50} of 88.38 μmol/L (Fig. 2D and E), whereas GRg1 displayed negligible interaction with CCR4 alone (Fig. 2F). Moreover, we used MST to determine more precise kinetic parameters of the GRg1−CKLF1 interaction. Changes in the thermophoretic signal yielded a K_D of 3.42 μmol/L for GRg1 binding to CKLF1 (Fig. 2G), which is consistent with the BLI assay results.

To elucidate the mechanism by which GRg1 inhibits the CKLF1−CCR4 interaction *via* binding to CKLF1, molecular docking and dynamics simulations were employed to predict the binding modes of CKLF1−GRg1 and CKLF1−CCR4, and to identify their respective key binding sites. These analyses revealed that Asn82, Ser84, and Gly19 of CKLF1 formed critical hydrogen bonds with the C6-glucosyl, C20-glucosyl, and C12-hydroxyl moieties of GRg1, respectively. Furthermore, Tyr87, Pro86, Pro83, Leu79, Lys78, Met23, and Ser16 contributed to a hydrophobic interaction network (Supporting Information Fig. S2A and S2B). Given that dammarane-type tetracyclic triterpenoid saponins (ginsenoside diol and triol types) primarily differ in substituents at the C3, C6, and C20 positions, and that the CKLF1-C27 functional domain (Ala73−Lys99) is crucial for CKLF1 biological activity[8,19], we speculate that the specific hydrogen bonds between the C6- and C20-glucosyl residues of GRg1 and the CKLF1-C27 domain underlie its inhibition of CKLF1 downstream signaling. Notably, NGR1, GRd, and GRe also possess C20-linked glucosyl groups, a glycosylation feature that potentially contributes to their observed inhibitory effects on CKLF1−CCR4 interaction. During 100 ns molecular dynamic simulations, we monitored the structural stability of CKLF1 and

way ANOVA followed by Tukey's *post hoc* test; data are presented as mean±SEM). (F) Schematic representation of the experimental protocol. CKLF1-rescue mice were established by intracerebroventricular injection of recombinant CKLF1 into *Cklf1*$^{-/-}$ mice. WT, *Cklf1*$^{-/-}$, and CKLF1-rescue mice underwent tMCAO, with reperfusion initiated 1.5 h post-occlusion. GRg1 was administered intragastrically during the occlusion phase, as well as at 24 and 48 h post-tMCAO. Two hours after the final dose, sMRI and behavioral assessments were performed. (G) Morphological characteristics of brain slices in WT, *Cklf1*$^{-/-}$, and CKLF1-rescue mice. (H, I) Cerebral infarction rate and edema rate ($n = 6$; $^{*}P < 0.05$, $^{**}P < 0.01$, $^{***}P < 0.001$; two-way ANOVA followed by Sidak's multiple comparison test, data are presented as mean±SEM).

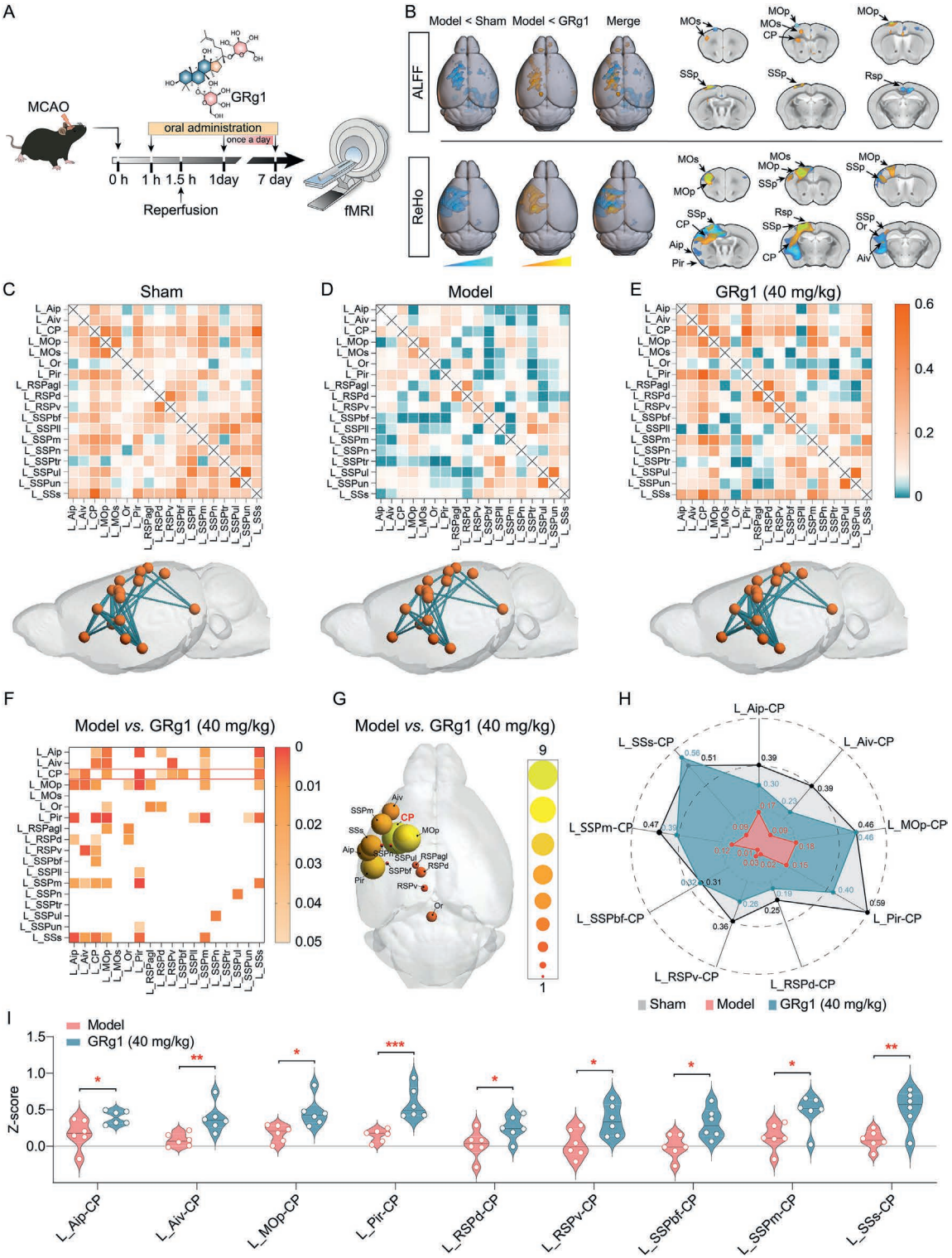

Figure 4 GRg1 restores brain functional connectivity post-tMCAO. (A) Schematic representation of the experimental protocol. fMRI scans were performed after 7 days of GRg1 treatment. (B) Alterations in ALFF and ReHo levels following tMCAO and the restorative effect of GRg1 were analyzed. For ALFF and ReHo analyses, the uncorrected voxel-level height threshold was set at $P < 0.01$. (C–E) Heatmaps and dot-line plots quantify FC strength among ROIs in each group, calculated using *Z*-scores. In the heatmaps, values are represented by color gradation, with warmer colors indicating higher FC strength. In the dot-line plots, line thickness denotes FC strength, with thicker lines reflecting greater values. (F) The matrix of FC with significant differences among ROIs between the model and GRg1 groups, with $P < 0.05$ as the threshold. (G) The count of functional connections exhibiting significant differences centered on different brain regions. (H) Mean *Z*-scores of CP to other ROIs in each

the CKLF1−GRg1 complex, as well as the number of hydrogen bonds. Our findings indicate that the interaction of GRg1 with CKLF1 exerts a minimal impact on the structural integrity of CKLF1, potentially underscoring the inherent stability of their complex (Fig. S2C). The hydrogen bond count exhibited fluctuations ranging from 0 to 11, predominantly stabilizing around an average of 4 (Fig. S2D), suggesting a strong binding between GRg1 and CKLF1. These simulations further revealed that Asn82, Ser84, and Asp71 of CKLF1 formed critical hydrogen bonds with Thr180, Glu181, Ser195, and Thr196 of CCR4, respectively (Fig. S2E). Notably, the CKLF1 residues Asn82 and Ser84, which interact with CCR4, overlap with those involved in GRg1 binding, supporting the hypothesis that GRg1 antagonizes CKLF1−CCR4 binding (Fig. S2F). Molecular dynamics simulations further indicate that GRg1 affects the structural stability of the CKLF1−CCR4 complex(Fig. S2G and S2H), underscoring its antagonistic role in this interaction. This interpretation is reinforced by a reduced number of hydrogen bonds between CCR4 and CKLF1 in the presence of GRg1 (Fig. S2I).

Because the production of IL-6 is closely regulated by CKLF1 and leads to the obstacle of clearing apoptotic neurons[19,27], we co-incubated BV-2 cells with CKLF1-C27 (1 μmol/L) and GRg1 (0.1−100 μmol/L) for 24 h to detect *Il6* mRNA levels. We observed that GRg1, at concentrations ranging from 1 to 100 μmol/L, effectively inhibited CKLF1-C27-induced *Il6* mRNA expression, with the most pronounced effect at 10 μmol/L (Fig. 2H). Hence, we established 10 μmol/L as the intervention dose of GRg1 *in vitro*. To further elucidate the bioactivity of GRg1, we evaluated its efficacy in modulating CKLF1-C27-induced calcium ion (Ca^{2+}) influx in HEK293-CCR4 cells[28], alleviating BV-2 microglial inflammation under both oxygen-glucose deprivation/reoxygenation (OGD/R) and non-OGD/R conditions, and inhibiting BV-2 microglial inflammation induced by conditioned medium from OGD/R-stimulated primary neurons. GRg1 exhibited significant inhibitory effects on CKLF1-C27-induced Ca^{2+} influx in HEK293-CCR4 cells (Fig. 2I−L), and attenuated inflammatory responses in BV-2 microglia (observed under both OGD/R and non-OGD/R conditions) (Supporting Information Fig. S3). Moreover, the conditioned medium from OGD/R-stimulated primary neurons, which had elevated CKLF1 content, significantly elicited inflammatory responses in primary microglia, whereas GRg1 exerted a marked anti-inflammatory effect (Fig. 2M−O). Collectively, these results indicate that GRg1 is a natural inhibitor of CKLF1.

3.3. GRg1 ameliorates ischemic/reperfusion injury post-tMCAO in a CKLF1-dependent manner

Considering the crucial role of CKLF1 in the pathogenesis, progression, and prognosis of AIS, we investigated the therapeutic efficacy of GRg1 (10−40 mg/kg) in ischemic brain injury using a tMCAO model. PNS and NBP administered intragastrically, as well as the CKLF1 antagonist peptide CKLF1-C19 *via* intracerebroventricular injection, were used as positive controls (Fig. 3A). Following confirmation of successful tMCAO by laser speckle imaging (Fig. 3B), structural MRI (sMRI), behavioral assessments, and histopathological evaluations were performed 48 h post-stroke. sMRI revealed that GRg1 treatment significantly attenuated structural brain damage, as evidenced by a marked reduction in infarct volume and edema ratio (Fig. 3C−E).

Neurological deficits were assessed by mNSS[17], focusing on impaired motor function, sensory acuity, balance, and reflexes in tMCAO mice. The results indicated significant sensorimotor impairment post-tMCAO, which was reversed by GRg1 treatment (Supporting Information Fig. S4A). Furthermore, behavioral analyses, including grip strength, grid walking, corner turning, and rotarod performance, demonstrated that GRg1 significantly improved sensorimotor function impaired by cerebral ischemia (Fig. S4B−S4E). Histological examination *via* HE and Nissl staining revealed significant necrosis, vacuolization, and a pronounced reduction in Nissl-stained neurons within the ischemic penumbra of tMCAO mice. Compared to the model group, GRg1 administration exhibited a marked attenuation of neuronal injury and an obvious increase in the number of Nissl-stained neurons (Supporting Information Fig. S5A−S5C). Taken together, these data indicate that GRg1 effectively mitigates both structural brain damage and associated functional deficits following AIS in a dose-dependent manner, with an optimal dosage of 40 mg/kg. Moreover, the therapeutic efficacy of GRg1 (40 mg/kg, i.g.) was comparable to that of PNS (100 mg/kg, i.g.), NBP (80 mg/kg, i.g.), or CKLF1-C19 (10 μg; ICV), highlighting its advantages in both dosage and administration route.

To track the tissue distribution of GRg1 administered orally in tMCAO mice, we developed a sensitive HPLC−MS/MS method for the simultaneous quantification of GRg1 and its three key metabolites (GRh1, GF1, and 20(*S*)-protopanaxatriol (PPT); Supporting Information Fig. S6A). Our data indicate that the surgical induction of tMCAO facilitates the transport of GRg1 across the blood−brain barrier into the cerebral parenchyma, supported by the significantly higher C_{max} (maximum observed concentration) and AUC_{0-last} (area under the curve from the time of dosing to the last measurable concentration) in the Ci (brain tissue ipsilateral to the infarction) region compared to the Cii (brain tissue contralateral to the infarction) and Ciii (corresponding brain tissue in sham mice) regions. The T_{max} (time of C_{max}) for Ci occurred 3 h after GRg1 administration, whereas T_{max} for Cii and Ciii was observed at 6 h (Fig. S6B−S6F). Furthermore, the AUC_{0-last} for GRh1 and GF1 was markedly greater in the Ci region than in the Cii and Ciii regions, while their T_{max} and C_{max} showed no significant changes (Fig. S6D−S6G). To clarify the interaction between CKLF1 and GRg1 metabolites (GRh1, GF1, and PPT), we employed BLI to determine their binding affinities. The results revealed that the K_D values followed the order: GRg1 (15.52 μmol/L) < GF1 (38.06 μmol/L) < GRh1 (71.81 μmol/L) < PPT (124.10 μmol/L), while the B_{max} values exhibited the trend: GRg1 (0.95 nm) >

group are illustrated in a radar chart. (I) Comparison of FC strength between the CP and other ROIs in the model and the GRg1 groups ($n = 6$; $^{*}P < 0.05$, $^{**}P < 0.01$, $^{***}P < 0.001$; one-way ANOVA followed by Tukey's *post hoc* test; data are presented as mean±SEM). Aip: Agranular insular area, posterior part; Aiv: Agranular insular area, ventral part; CP: Caudoputamen; MOp: Primary motor area; MOs: Secondary motor area; Or: Optic radiation; Pir: Piriform area; RSP: Retrosplenial area (agl: lateral agranular part, d: dorsal part, v: ventral part); SSP: Primary somatosensory area (bf: barrel field, ll: lower limb, m: mouth, n: nose, tr: trunk, ul: upper limb, un: unassigned); SSs: Supplemental somatosensory area.

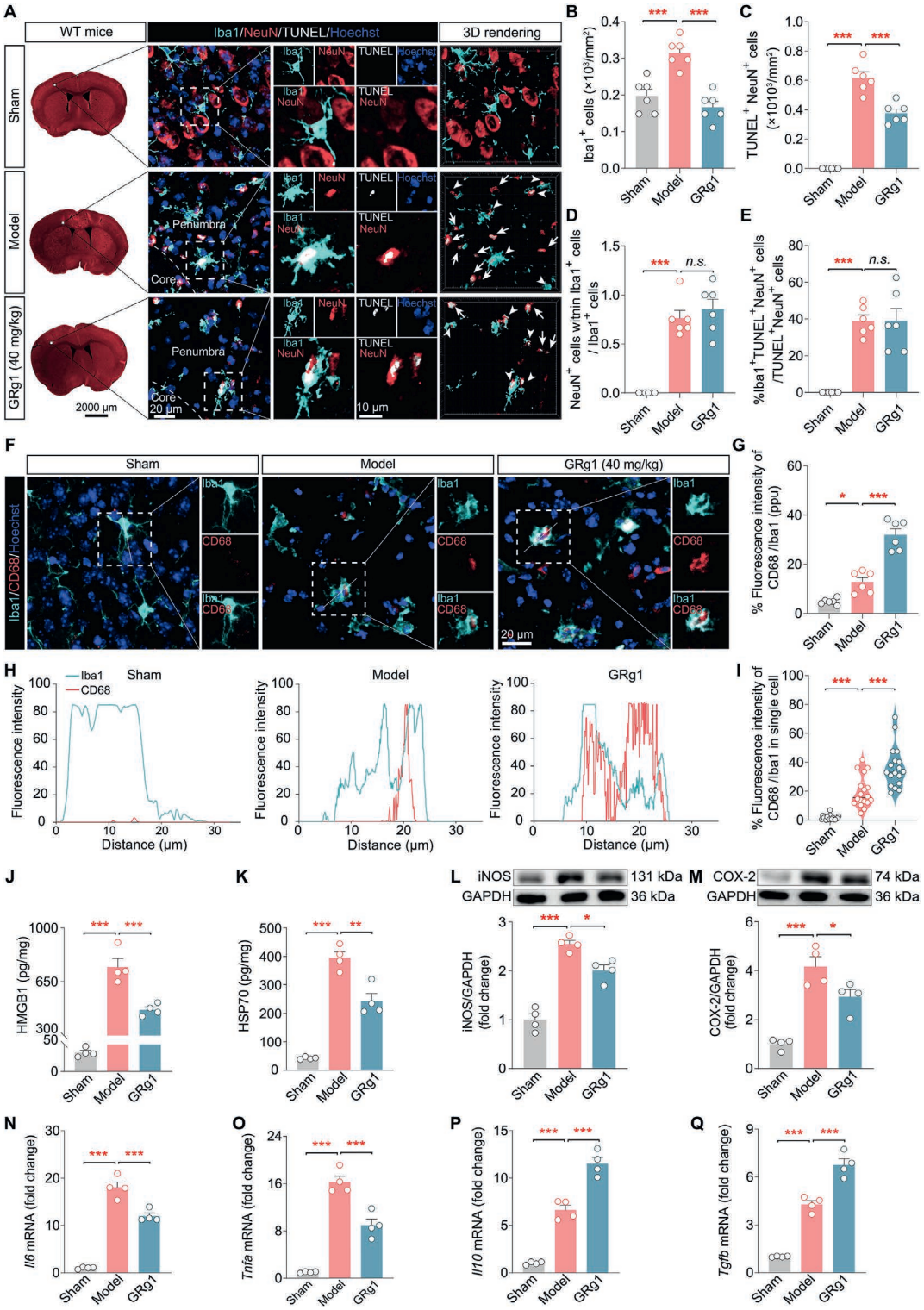

Figure 5 GRg1 enhances TUNEL $^{+}$ neurons clearance and reduces DAMPs release following tMCAO. (A) Representative immunofluorescence colocalization images of microglial marker Iba1 (cyan), neuronal marker NeuN (red), dead/dying cell marker TUNEL (white), and nuclear marker Hoechst 33342 (blue) in peri-infarct areas. The white arrowheads indicate dead/dying neurons that have been internalized by microglia ($Iba1^{+}NeuN^{+}TUNEL^{+}$), and white arrows indicate dead/dying neurons not yet engulfed ($Iba1^{-}NeuN^{+}TUNEL^{+}$). Three-dimensional (3D) rendering z-stack projections were generated using confocal Z-stacks (9 serial sections acquired at a z-step interval of 2.2 μm). (B, C) Number of microglia and dead/dying neurons in the penumbra region ($n = 6$ mice, $^{***}P < 0.001$, one-way ANOVA followed by Tukey's *post hoc* test). (D) Weighted internalizing capacity of microglia was quantified as the percentage of engulfed neurons relative to the total number of microglia (number of $NeuN^{+}$ cells within $Iba1^{+}$ cells/$Iba1^{+}$ cells); $n = 6$ mice, n.s.: non-significant, $^{***}P < 0.001$; one-way ANOVA followed by Tukey's *post hoc* test. (E) Proportion of engulfed $TUNEL^{+}$ neurons to total $TUNEL^{+}$ neurons, calculated as the percentage of $Iba1^{+}TUNEL^{+}NeuN^{+}$ cells

GRh1 (0.86 nm) > PPT (0.83 nm) > GF1 (0.45 nm) (Fig. S6H−S6K). These findings further suggest that the anti-cerebral ischemia effect of GRg1 targeting CKLF1 may primarily depend on the parent compound rather than its metabolites.

To investigate the role of CKLF1 in the anti-stroke effect of GRg1, we established a tMCAO model in WT and *Cklf1*$^{-/-}$ mice, which were subsequently treated with GRg1 followed by sMRI scanning (Fig. 3F−I), behavioral tests (Supporting Information Fig. S7), and cerebral blood perfusion imaging (Supporting Information Fig. S8). The results demonstrated that CKLF1 deletion significantly alleviated acute ischemic brain injury, improved behavioral deficits, and enhanced cerebral blood flow post-tMCAO. To further verify whether GRg1's therapeutic effects on ischemic stroke are dependent on CKLF1, we generated CKLF1-rescue mice by administering CKLF1 *via* intracerebroventricular injection into *Cklf1*-KO mice. Notably, this rescue intervention restored the anti-ischemic brain injury effects of GRg1 that were absent in *Cklf1*-KO mice prior to rescue (Fig. 3F−I, Fig. S7), suggesting that GRg1 ameliorates ischemic/reperfusion injury post-tMCAO in a CKLF1-dependent manner.

3.4. GRg1 restores brain functional connectivity post-tMCAO

To comprehensively assess the neurorestorative effects of GRg1 against ischemic brain injury comprehensively, we conducted functional MRI (fMRI) to evaluate the brain functional connectivity (FC) in tMCAO mice after a 7-day treatment regimen (Fig. 4A). Amplitude of low-frequency fluctuations (ALFF) and regional homogeneity (ReHo), data-driven measures that reflect the amplitude and coordination of regional neuronal activity, respectively, were used to quantify spontaneous neural activity based on blood oxygen level-dependent (BOLD) signals[15]. In tMCAO mice, significant reductions in both ALFF and ReHo levels were predominantly observed in the ischemic hemisphere compared to sham-operated controls. Specifically, ALFF levels were notably diminished in both the primary motor area (MOp) and secondary motor area (MOs), as well as in the primary somatosensory area (SSp) and retrosplenial area (Rsp). Similarly, ReHo exhibited reductions in MOp, MOs, SSp, caudoputamen (CP), Rsp, optic radiation (Or), and agranular insular area (Ai). Treatment with GRg1 facilitated the recovery of ALFF and ReHo metrics in the MOp, MOs, CP, and SSp (Fig. 4B), which are typically affected by tMCAO[29].

Extending these findings, we selected specific regions of interest (ROIs) for a comprehensive ROI-wise FC analysis. Our data revealed a reduction in FC among the ROIs after tMCAO, whereas GRg1 administration enhanced FC between these compromised regions (Fig. 4C−E). The CP, a critical component of the lesion core in the transient occlusion model, exerts a major impact on stroke outcomes[29,30]. Notably, GRg1 administration strengthened connections between the CP and various brain regions, particularly those linked to motor function, sensory acuity, and cognitive processes (Fig. 4F−I). The mean *Z*-score of FC showed a marked enhancement in connection strength following GRg1 treatment, as illustrated by the radar chart (Fig. 4H) and violin plot (Fig. 4I). These fMRI findings provide further support for the observed improvements in behavioral performance associated with GRg1 treatment, suggesting a potential for network-level neuronal restoration.

3.5. GRg1 reduces dead/dying neuron density and DAMP release in AIS

To investigate whether GRg1 promotes dead/dying neuron clearance following AIS, we initially selected the peri-infarct region (the area surrounding the infarct core, which contains abundant apoptotic neurons) to directly compare the efficiency of apoptotic neuron clearance between the model and GRg1 groups. We then performed immunofluorescence labeling using Iba1, NeuN, and TUNEL to identify microglia, neurons, and dead/dying cells, respectively (Fig. 5A). GRg1 administration significantly reduced the number of both microglia (Iba1$^+$ cells, Fig. 5B) and dead/dying neurons (NeuN$^+$TUNEL$^+$ cells, Fig. 5C) within the ischemic penumbra. Interestingly, despite the reduction in dead/dying neurons, GRg1 treatment did not markedly increase the weighted internalizing capacity (Iba1$^+$NeuN$^+$ cells/Iba1$^+$ cells, Fig. 5D) of microglia or the proportion of engulfed dead/dying neurons (% Iba1$^+$TUNEL$^+$NeuN$^+$ cells/TUNEL$^+$NeuN$^+$ cells, Fig. 5E). To elucidate this phenomenon, we considered that phagocytosis comprises three distinct phases, recognition/binding, internalization, and digestion, each of which is regulated separately by phagocytes[5]. We hypothesize that GRg1 potentiates the role of microglia in the degradation of dead/dying cells, thereby promoting dead/dying neuron clearance. CD68, a biomarker of microglial lysosomal activity, reflects microglial degradation during phagocytosis[31]. As expected, we found upregulated microglial CD68 expression in GRg1-treated mice compared to model animals (Fig. 5F−I).

We further assessed the levels of HMGB1 and heat shock protein 70 (HSP70), which are well-established DAMP released from dead/dying neurons[32], in the peri-infarct samples. Our findings indicated that both HMGB1 and HSP70 levels were significantly elevated in the model group compared to the sham group, with this increase notably attenuated by GRg1 treatment (Fig. 5J and K). The reduction in DAMP concentrations corresponded to a marked alleviation of neuroinflammation, as evidenced by the markedly lower levels of key inflammation-related enzymes (iNOS and COX-2, Fig. 5L and M) and pro-inflammatory factors (*Il6* and *Tnfa*, Fig. 5N and O), coupled

to TUNEL$^+$NeuN$^+$ cells; n = 6 mice, n.s.: non-significant, $^{***}P < 0.001$; one-way ANOVA followed by Tukey's *post hoc* test. (F) Representative immunofluorescence images showing lysosomal activity (CD68$^+$, red) in microglia (Iba1$^+$, cyan). (G) Quantification of CD68 expression as the ratio of CD68 intensity to Iba1 intensity in parts per unit (ppu); $n = 6$ mice; $^{*}P < 0.05$ and $^{***}P < 0.001$, one-way ANOVA followed by Tukey's *post hoc* test. (H) Iba1 and CD68 fluorescence intensities were quantified along the white lines in representative microglia. (I) Ratio of CD68 intensity to Iba1 intensity in individual cells ($n = 18$ cells; $^{***}P < 0.001$; one-way ANOVA followed by Tukey's *post hoc* test). (J, K) HMGB1 and HSP70 levels in peri-infarct brain tissues ($n = 4$ mice, $^{**}P < 0.01$, $^{***}P < 0.001$; one-way ANOVA followed by Tukey's *post hoc* test). (L, M) iNOS and COX-2 levels in peri-infarct brain tissues ($n = 4$ mice, $^{*}P < 0.05$, $^{***}P < 0.001$; one-way ANOVA followed by Tukey's *post hoc* test). (N−Q) mRNA levels of inflammatory cytokines (*Il6*, *Tnfa*, *Il10*, *Tgfb*) in penumbra tissues ($n = 4$ mice, $^{*}P < 0.05$, $^{***}P < 0.001$; one-way ANOVA followed by Tukey's *post hoc* test). All data are expressed as the mean±SEM.

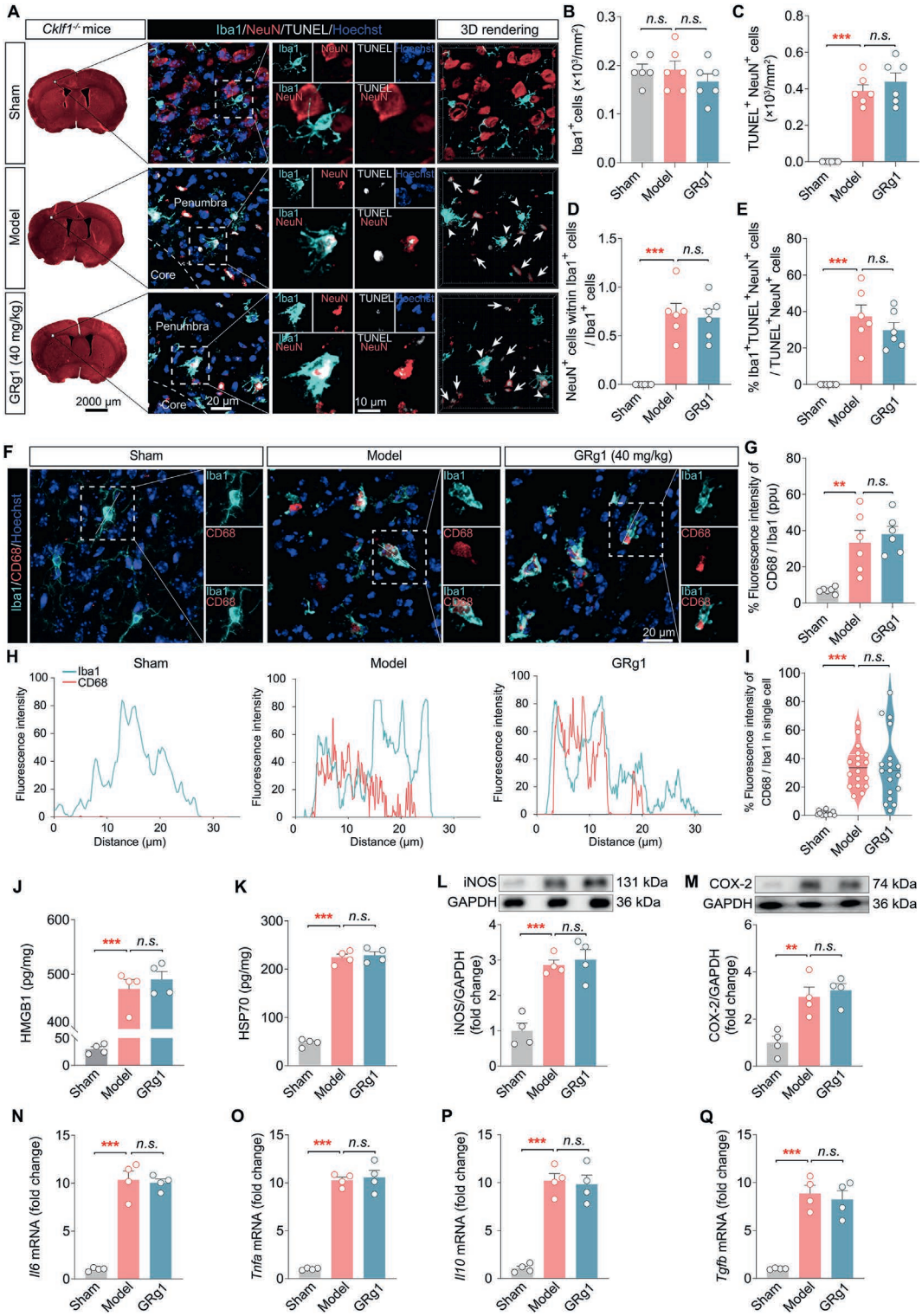

Figure 6 CKLF1 deficiency abolishes GRg1-enhanced dead/dying neuron clearance following tMCAO. (A) Representative immunofluorescence colocalization images of microglial marker Iba1 (cyan), neuronal marker NeuN (red), dead/dying cell marker TUNEL (white), and nuclear marker Hoechst 33342 (blue) in peri-infarct areas of *Cklf1*$^{-/-}$ mice. The white arrowheads indicate dead/dying neurons that have been internalized by microglia (Iba1^{+}NeuN^{+}TUNEL^{+}), and white arrows indicate dead/dying neurons not yet engulfed (Iba1^{-}NeuN^{+}TUNEL^{+}). (B, C) Number of microglia and dead/dying neurons in the penumbra region ($n = 6$ mice; n.s.: non-significant, $^{***}P < 0.001$; one-way ANOVA followed by Tukey's *post hoc* test). (D) Weighted internalizing capacity of microglia ($n = 6$ mice, n.s.: non-significant, $^{***}P < 0.001$; one-way ANOVA followed by Tukey's *post hoc* test). (E) Proportion of engulfed TUNEL^{+} neurons to total TUNEL^{+} neurons ($n = 6$ mice; n.s.: non-significant,

with a significant increase in anti-inflammatory factors (*Il10* and *Tgfb*, Fig. 5P and Q) within the penumbral region of mice treated with GRg1. Additionally, GRg1 treatment decreased the proportion of pro-inflammatory microglial phenotypes (Supporting Information Fig. S9A and S9B) while increasing the proportion of anti-inflammatory microglial phenotypes (Fig. S9C and S9D), indicating that GRg1 modulates microglial polarization toward an anti-inflammatory type following ischemia. To investigate the relationship between microglial polarization and lysosomal activity following stroke, we analyzed the correlation between CD16/CD68 and CD206/CD68 within individual cells, using a statistical sample of 20 randomly selected cells from the model and GRg1 groups (10 cells per group) (Fig. S9E−S9H). The analysis showed a negative correlation between CD16 and CD68, and a positive correlation between CD206 and CD68 in microglia after stroke. This result indicates that enhanced lysosomal activity/degradation in microglia facilitates their polarization toward an anti-inflammatory phenotype.

Taken together, these data suggest that GRg1 may impede microglial recruitment to the penumbra while enhancing the capacity of microglia to degrade engulfed cargo, leading to accelerated clearance of dead/dying neurons, decreased release of DAMP, and alleviated neuroinflammation.

3.6. CKLF1 deficiency abolishes the clearance of dead/dying neurons enhanced by GRg1

Immunofluorescence analysis of dead/dying neuron clearance (Fig. 6A−E) in the context of CKLF1 deletion revealed that GRg1 treatment did not lead to significant changes in microglial density, the number of TUNEL$^+$ neurons, the weighted internalizing capacity of microglia, or the proportion of engulfed dead/dying neurons. Additionally, we evaluated the expression of CD68 in microglia within the ischemic penumbra, observing that *Cklf1* knockout abrogated the GRg1-induced upregulation of CD68 levels (Fig. 6F−I).

Likewise, CKLF1 deletion effectively silenced the downregulated effect of GRg1 on DAMP (HMGB1 and HSP70), key inflammatory proteins (iNOS and COX-2), and pro-inflammatory cytokines (*Il6* and *Tnfa*), while concurrently eliminating the GRg1-induced upregulation of anti-inflammatory mediators (*Il10* and *Tgfb*) (Fig. 6J−Q). These findings underscore that CKLF1 deficiency abolishes GRg1-mediated enhancement of dead/dying neuron clearance, thereby hinders the resolution of neuroinflammation in AIS.

3.7. GRg1 antagonizes CKLF1-C27-induced microglial transmigration and degradation dysfunction

Since CKLF1 promotes microglial infiltration into the ischemic penumbra *via* the CCR4[10] and GRg1 effectively disrupts CKLF1−CCR4 binding, we hypothesized that the reduced microglial density in the penumbra after GRg1 treatment may be due to the inhibitory effects of GRg1 on CKLF1-induced microglial infiltration. To validate this hypothesis, we conducted a transwell experiment (Fig. 7A). Results demonstrated that CKLF1-C27 significantly promoted the transmigration of BV-2 microglia, whereas the presence of GRg1 abolished this effect (Fig. 7B). Cytochalasin D (Cyto D) was used as a positive control to inhibit actin polymerization and block CKLF1-C27-induced migration (Fig. 7B). Collectively, these findings suggest that GRg1 reduces microglial density in the penumbra by impeding the CKLF−CCR4 chemotactic axis (Fig. 7C).

Efficient degradation by phagocytes is a crucial step in mitigating the inflammatory response during efferocytosis, which is primarily facilitated by lysosomes. As illustrated in Fig. 5F−I, GRg1 administration resulted in the notable upregulation of CD68, an indicator of lysosomal activity. These findings imply that GRg1 may contribute to enhancing lysosomal function. To confirm this hypothesis, a co-culture system of BV-2 microglia and apoptotic SH-SY5Y cells was utilized to assess cargo degradation, lysosomal morphological characteristics, lysosomal membrane permeabilization (LMP), and lysosomal acidification (Fig. 7D). Notably, CKLF1-C27-treated BV-2 cells (with or without OGD/R) exhibited increased cargo retention over time, suggesting CKLF1-C27 impaired lysosomal cargo processing, which was reversed by GRg1 (Fig. 7E and F, Supporting Information Fig. S10A−S10C). Furthermore, GRg1 significantly inhibited CKLF1-C27-induced microglial inflammation during efferocytosis, as demonstrated by reduced mRNA expression of pro-inflammatory cytokines (*Il6* and *Tnfa*) and elevated mRNA expression of anti-inflammatory cytokines (*Il10* and *Tgfb*) (Supporting Information Fig. S11A and S11B).

Lysosomes can be classified into three categories based on their diameter: normal lysosomes (< 1.0 μm), intermediate lysosomes (1.0−2.5 μm), and abnormal lysosomal vacuoles (> 3.0 μm)[33]. In the vehicle, GRg1, and CKLF1-C27 + GRg1 groups, most lysosomes exhibited diameters of less than 3 μm, whereas a notable presence of larger lysosomes was observed following exposure to CKLF1-C27, suggesting CKLF1-C27 induces lysosomal dysfunction. Furthermore, GRg1 mitigates the lysosomal dysfunction induced by CKLF1-C27 (Fig. 7G−I). LMP is an important manifestation of lysosomal impairment that can be triggered by various cytotoxic stimuli and cellular conditions. Lysosomal rupture exposes its inner luminal glycans, which are specifically recognized by galectin-3 (LGALS3), making LGALS3 currently the most reliable biomarker for detecting LMP[34,35]. CKLF1-C27 treatment significantly augmented the colocalization of LGALS3 with LAMP1, a lysosomal marker, leading to a marked increase in the percentage of LGALS3 puncta-positive cells (Fig. 7J and K, Fig. S10D and S10E). In contrast, GRg1 attenuated the CKLF1-C27-induced increase in the number of LGALS3-positive cells. These observations indicate

$^{***}P < 0.001$; one-way ANOVA followed by Tukey's *post hoc* test). (F) Representative immunofluorescence images showing lysosomal activity (CD68$^+$, red) in microglia (Iba1$^+$, cyan). (G) Quantification of CD68 expression ($n = 6$ mice; n.s.: non-significant, $^{**}P < 0.01$; one-way ANOVA followed by Tukey's *post hoc* test). (H) Iba1 and CD68 fluorescence intensities were quantified along the white lines in representative microglia. (I) Ratio of CD68 intensity to Iba1 intensity in individual cells ($n = 18$ cells, n.s.: non-significant, $^{**}P < 0.01$; one-way ANOVA followed by Tukey's *post hoc* test). (J, K) HMGB1 and HSP70 levels in peri-infarct brain tissues ($n = 4$ mice, $^{***}P < 0.001$, one-way ANOVA followed by Tukey's *post hoc* test). (L, M) iNOS and COX-2 expression levels in peri-infarct brain tissues ($n = 4$ mice, $^{**}P < 0.01$, $^{***}P < 0.001$; one-way ANOVA followed by Tukey's *post hoc* test). (N−Q) mRNA levels of inflammatory cytokines (*Il6*, *Tnfa*, *Il10*, *Tgfb*) in penumbra tissues ($n = 4$ mice, $^{***}P < 0.001$; one-way ANOVA followed by Tukey's *post hoc* test). All data are expressed as the mean±SEM.

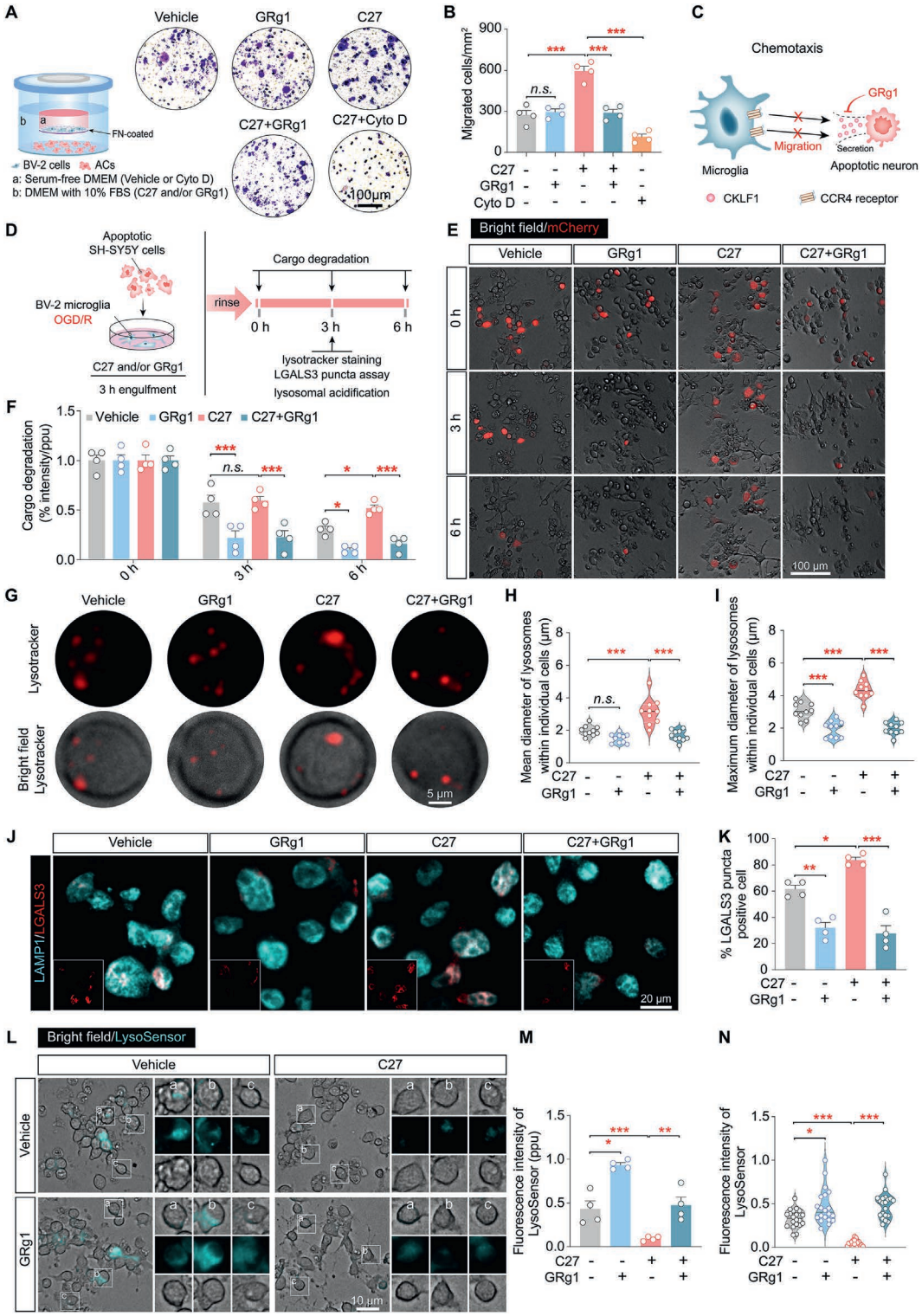

Figure 7 GRg1 inhibits CKLF1-C27-induced microglial transmigration and degradation dysfunction. (A) Schematic of the transwell migration assay and representative crystal violet-stained images of migrated BV-2 microglia. BV-2 cells were evaluated for transmigration capacity following exposure to vehicle or Cyto D (50 μmol/L) in serum-free medium, migrating toward ACs co-incubated with GRg1 (10 μmol/L) and/or CKLF1-C27 (1 μmol/L) in serum-containing medium (10% FBS). (B) After 24 h, migrated cells on the bottom of the chamber were stained with crystal violet for counting ($n = 4$; $^{***}P < 0.001$; one-way ANOVA followed by Tukey's *post hoc* test). (C) Schematic illustrating how GRg1 impedes the chemotactic recognition of ACs by microglia. CKLF1, secreted by apoptotic neurons, promotes microglial migration toward ACs via

that GRg1 can reinstate microglial lysosomal function compromised by CKLF1-C27. We also investigated the role of CKLF1-C27 in lysosomal acidification, a crucial process for lysosomal functionality. BV-2 microglia were treated with CKLF1-C27 and/or GRg1 in the presence of ACs for a duration of 3 h, rinsed to remove non-internalized ACs, incubated for another 3 h, and then exposed to a medium containing 1 μmol/L LysoSensor Green DND-189 for 30 min. Our data revealed that GRg1 significantly reversed the CKLF1-C27-mediated reduction in LysoSensor fluorescence intensity in BV-2 microglia, indicating that GRg1 attenuates the inhibitory effect of CKLF1-C27 on lysosomal acidification (Fig. 7L−N, Fig. S10F−S10H). Consequently, GRg1 mitigates CKLF1-C27-induced impairment of microglial lysosomal function.

3.8. GRg1 promotes microglial degradation via the mTORC1/TFEB pathway

To investigate the mechanism by which GRg1 enhances microglial degradation, we examined the role of TFEB, a master regulator of lysosomal biogenesis and function.[36,37]. TFEB activity is regulated by phosphorylation, which retains TFEB in the cytoplasm in an inactive state. Upon dephosphorylation, TFEB translocates to the nucleus to activate target gene transcription. Our results indicate that CKLF1-C27 inhibits microglial TFEB activation during efferocytosis, as evidenced by reduced nuclear translocation. Conversely, GRg1 reverses this inhibition (Fig. 8A−C, Supporting Information Fig. S12A−S12C). Additionally, GRg1 counteracts the CKLF1-C27-induced decline in the mRNA levels of TFEB target genes *Mcoln1*, *Atp6v1h*, *Atp6v0d1*, *Ctsb*, and *Ctsf* (Fig. 8D). MCOLN1 functions as a lysosomal calcium channel that initiates the eventual fusion of lysosomes with the plasma membrane, whereas ATP6V1H and ATP6V0D1 are involved in lysosomal acidification. CTSB and CTSF are lysosomal hydrolases crucial for lysosomal degradation.

TFEB nuclear localization inhibition is generally caused by mTORC1 activation and subsequent TFEB phosphorylation[37]. Upon activation, mTOR is phosphorylated at several residues, notably Thr2446, Ser2448, and Ser2481, with Ser2448 being the predominant site in mTORC1[38]. We observed increased mTOR phosphorylation (Ser2448) and TFEB phosphorylation (Ser211) in CKLF1-C27-treated BV-2 microglia undergoing efferocytosis , conversely, GRg1 significantly decreased these phosphorylation levels (Fig. 8E and F, Fig. S12D−S12F). This was corroborated by *in vivo* data, which showed that compared with the model group, GRg1 decreased the phosphorylation levels of mTOR (Ser2448) and TFEB (Ser211), thereby promoting TFEB activation (Supporting Information Fig. S13A−S13C).

For further validation, we generated *Ccr4*-KO BV-2 cell lines using CRISPR/Cas9 to assess TFEB activation and the phosphorylation levels of mTOR (Ser2448) and TFEB (Ser211) during efferocytosis (Fig. 8A, Fig. S13D). Our data demonstrates that treatment with CKLF1-C27 and/or GRg1 in *Ccr4*-KO BV-2 microglia produced no significant changes in TFEB activation (Fig. 8G and H) or in the phosphorylation of mTOR (Ser2448) and TFEB (Ser211) (Fig. S13E−S13G). These results indicate that GRg1 targets CKLF1 to activate TFEB *via* CCR4. Additionally, we examined the effect of rapamycin, a selective mTORC1 inhibitor[39], on CKLF1-C27-induced biological changes in BV-2 microglia during efferocytosis. Our results indicated that rapamycin significantly reversed the CKLF1-C27-mediated impairment of degradation, suppression of TFEB activation, and increases in mTOR and TFEB phosphorylation in BV-2 microglia during efferocytosis (Fig. S13I−S13K, Fig. 8I and J). In the presence of rapamycin, GRg1 exerted no significant effect on degradation, TFEB activation, or the phosphorylation of mTOR and TFEB. Moreover, *Tfeb*-KO abolished the effects of CKLF1-C27 and/or GRg1 on the phagocytic degradation of BV-2 microglia (Fig. 8K and L, Fig. S13H). Taken together, GRg1 targets CKLF1 to inhibit CCR4-dependent signaling, thereby suppressing mTOR phosphorylation and promoting TFEB nuclear translocation (Fig. 8M).

CCR4 is also expressed on neurons, and the direct effects of GRg1 on injured neurons post-stroke remain unclear. To address this question, we first assessed CCR4 expression on neurons within the peri-infarct region and observed its significant upregulation in ischemic neurons, while GRg1 did not affect CCR4 expression. We then subjected primary neurons from *Cklf1*$^{-/-}$ mice to OGD/R and assessed the influence of CKLF1-C27, CCL17 (a CCR4-specific agonist ligand), and/or GRg1 on cell viability, as well as on levels of the apoptotic marker cleaved caspase-3 (cCasp3) and the anti-apoptotic protein BCL2. The data show that GRg1 failed to significantly alleviate OGD/R-induced injury in *Cklf1*-KO primary neurons. In contrast, CKLF1-C27 and CCL17 aggravated injury in these neurons after

CCR4. GRg1 exerts its inhibitory effect on microglial migration by disrupting the CKLF1/CCR4 axis. (D) Experimental design for cargo degradation and lysosomal function analysis. BV-2 microglia were subjected to OGD/R (2 h of OGD followed by reoxygenation) and co-cultured with apoptotic SH-SY5Y-mCherry cells for 3 h. During this co-culture, GRg1 (10 μmol/L) and/or CKLF1-C27 (1 μmol/L) were administered as interventions. After treatment, cells were gently washed to remove non-internalized ACs. Real-time fluorescence imaging was conducted over 6 h (0−6 h) using confocal microscopy. The experimental protocols for LysoTracker staining, LGALS3 puncta assay, and lysosomal acidification were consistent with those used for cargo degradation analysis, except that apoptotic cells were derived from SH-SY5Y cells and detection was performed 3 h after rinsing. (E) Representative images of efferocytosis BV-2 microglia at 0, 3, and 6 h after washout of non-internalized ACs. (F) Quantification of apoptotic SH-SY5Y cell degradation in efferocytosis BV-2 microglia. AC counts at 0 h in each group were normalized to 1, respectively ($n = 4$, $^{*}P < 0.05$, $^{***}P < 0.001$, n.s.: non-significant; two-way ANOVA, Sidak's multiple comparison test). (G) Lysosomal morphological analysis was assessed by Lysotracker staining. (H, I) Mean and maximum lysosome diameters within individual cells ($n = 10$ cells, $^{***}P < 0.001$, n.s.: non-significant; one-way ANOVA followed by Tukey's *post hoc* test), respectively. (J) Representative images of immunofluorescence colocalization of LAMP1 (cyan) and LGALS3 (red) in BV-2 cells. (K) Proportion of LGALS3 puncta-positive cells to total cells ($n = 4$ random fields; $^{*}P < 0.05$, $^{**}P < 0.01$, $^{***}P < 0.001$; one-way ANOVA followed by Tukey's *post hoc* test). (L) Lysosomal acidification was assessed using LysoSensor Green DND-189. (M) Fluorescence intensity of LysoSensor within parts per unit ($n = 4$ random fields; $^{*}P < 0.05$, $^{**}P < 0.01$, $^{***}P < 0.001$; one-way ANOVA followed by Tukey's *post hoc* test). (N) Fluorescence intensity of LysoSensor in individual cells ($n = 20$ cells; $^{*}P < 0.05$, $^{***}P < 0.001$; one-way ANOVA followed by Tukey's *post hoc* test). All data are expressed as the mean±SEM.

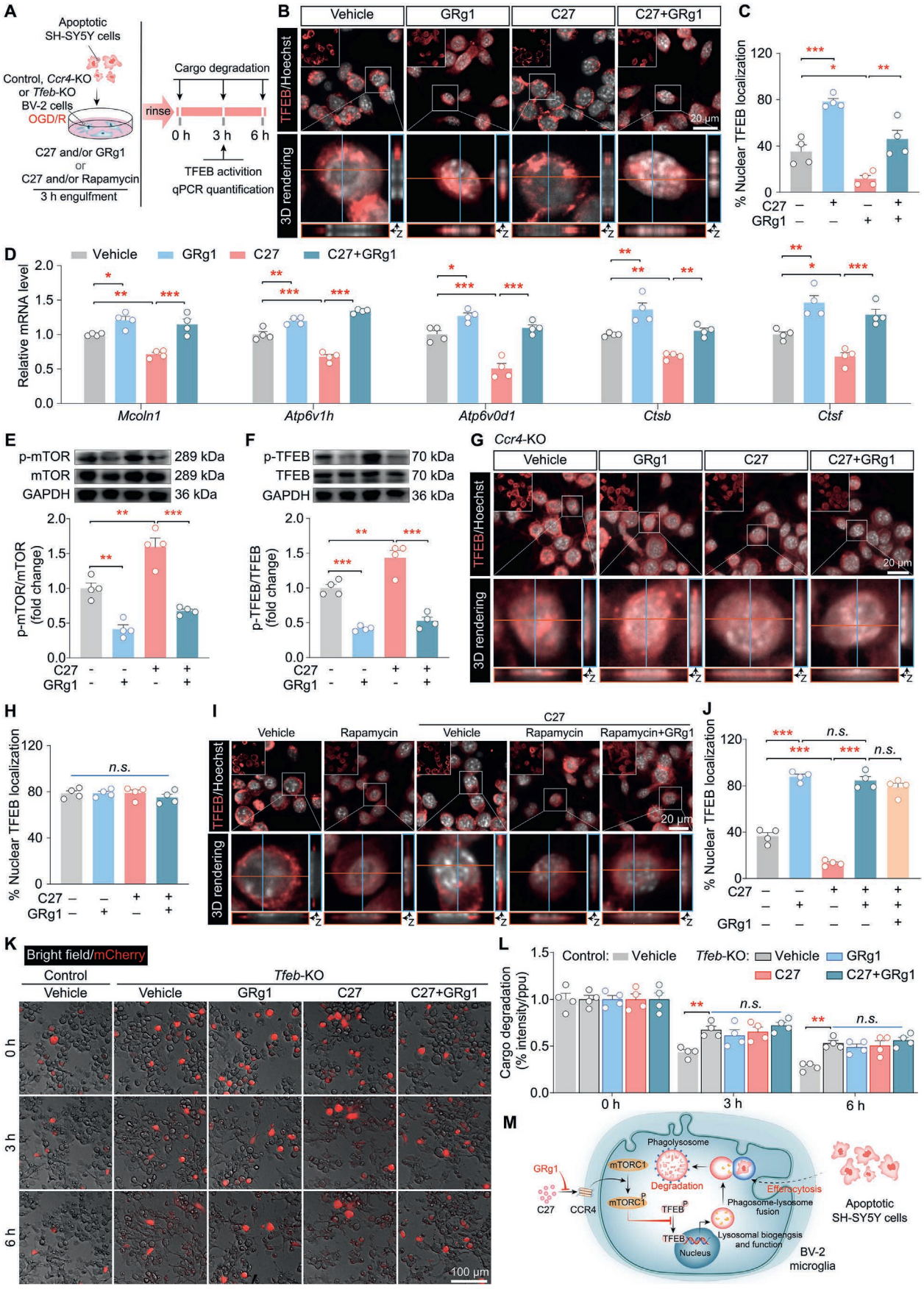
A
Apoptotic SH-SY5Y cells
Control, Ccr4-KO or Tfeb-KO BV-2 cells
OGD/R
C27 and/or GRg1 or C27 and/or Rapamycin
3 h engulfment
rinse
Cargo degradation
0 h 3 h 6 h
TFEB activition
qPCR quantification
B
Vehicle
GRg1
C27
C27+GRg1
TFEB/Hoechst
3D rendering
20 μm
C
% Nuclear TFEB localization
C27
GRg1
D
Vehicle
GRg1
C27
C27+GRg1
Relative mRNA level
Mcoln1
Atp6v1h
Atp6v0d1
Ctsb
Ctsf
E
p-mTOR
mTOR
GAPDH
289 kDa
36 kDa
p-mTOR/mTOR (fold change)
F
p-TFEB
TFEB
70 kDa
p-TFEB/TFEB (fold change)
G
Ccr4-KO
H
n.s.
I
Rapamycin
Rapamycin+GRg1
J
K
Bright field/mCherry
Control
Tfeb-KO
0 h
3 h
6 h
100 μm
L
Control: Vehicle
Tfeb-KO: Vehicle GRg1 C27 C27+GRg1
Cargo degradation (% intensity/ppu)
M
Phagolysosome
mTORC1
Degradation
Efferocytosis
GRg1
C27
CCR4
Phagosome-lysosome fusion
TFEB
Lysosomal biogenesis and function
Nucleus
Apoptotic SH-SY5Y cells
BV-2 microglia

OGD/R. Although GRg1 markedly reversed CKLF1-C27-induced injury, it did not suppress neuronal injury triggered by CCL17. These results indicate that the neuroprotective effect of GRg1 also relies on inhibiting CKLF1-mediated CCR4 activation.

4. Discussion

Efficient clearance of dead/dying neurons is essential for resolving neuroinflammation following AIS, which is markedly impaired by CKLF1. Here, we describe a novel strategy for identifying CKLF1 inhibitors from PNS through the integrated use of BLI-fishing, LC−MS/MS identification, and NanoBRET validation. Among the candidates, GRg1 exhibits the highest affinity for CKLF1 and the most potent inhibitory efficacy against the CKLF1−CCR4 interaction, effectively suppressing CKLF1-C27 peptide-induced calcium influx and cytokine production. In experimental AIS models, GRg1 confers neuroprotective effects by mitigating ischemic brain damage and promoting neuronal functional recovery. Mechanistically, GRg1 binds to CKLF1 and modulates the mTORC1/TFEB pathway to enhance lysosomal function, thereby facilitating the clearance of dead/dying neurons. Together, these findings present an efficient approach for discovering natural CKLF1 inhibitors and highlight GRg1 as a promising candidate for enhancing dead/dying neuron clearance in AIS.

Neuroinflammation is among the most critical mechanisms in the cascade of acute cerebral ischemic injury[40]. Upon AIS onset, focal brain ischemia elicits neuronal death, leading to the uncontrolled release of DAMP[41]. These DAMP subsequently initiate inflammatory responses *via* pattern recognition receptors (PRRs)[42], which in turn exacerbate neuronal death and form a vicious cycle. The resulting inflammatory microenvironment promotes microglial polarization toward the pro-inflammatory phenotype, and pro-inflammatory microglia further secrete pro-inflammatory cytokines that intensify neuroinflammation, thereby amplifying the vicious circle. Thus, impaired clearance of apoptotic neurons acts as both an initiator and amplifier of the acute inflammatory storm following ischemic stroke, and identifying therapeutic agents that facilitate the clearance of apoptotic neurons holds substantial potential for the management of ischemic stroke. Microglia, the resident immune sentinels of the cerebral parenchyma, act as both the primary effectors of neuroinflammation and the main executors of dead/dying neuron clearance within 48 h post-stroke[10,43]. It is well established that impaired microglial efferocytosis results in increased neuronal death in rodent models of ischemic stroke[10,22]. Our prior research has demonstrated that CKLF1 induces dysfunction of microglial efferocytosis and promotes acute neuroinflammation[10,19]. Specifically, pre-stroke intracerebral administration of the CKLF1-C27 peptide exacerbates M1-type microglial polarization and amplifies neural injury. Conversely, genetic knockout of *Cklf1* significantly attenuates post-stroke neuroinflammation and reduces the number of apoptotic neurons. These findings highlight CKLF1 inhibition as a potential therapeutic strategy to enhance the clearance of dead/dying neurons and mitigate post-stroke inflammatory sequelae.

Currently, Xuesaitong (*Panax notoginseng* saponins) has been extensively applied in clinical practice for the treatment of AIS[44]. The mechanisms by which it improves cerebral ischemic injury mainly include anti-neuroinflammatory effects[12] and the reduction of dying neurons[13]. Guided by CKLF1's established role in ischemic stroke pathogenesis and the pharmacological characteristics of PNS against cerebral ischemia, we postulated that PNS contains natural CKLF1 inhibitors. However, the complex components in *Panax notoginseng* saponins hinder the discovery of bioactive compounds. To overcome this dilemma, this study established an efficient drug discovery system targeting CKLF1, which integrates BLI fishing, LC−MS/MS identification, and NanoBRET screening, and identified GRg1 as the optimal candidate.

During AIS, clearance of dead/dying neurons by microglia involves a multistage process. CKLF1 recruits microglia to the ischemic penumbra through the CKLF1−CCR4 chemotactic axis and augments microglial internalization of dead/dying neurons *via* the IL-6/STAT3/Vav1/Rac1 signaling pathway. However, it concurrently disrupts lysosomal function, inducing a degradation impairment that leads to cargo accumulation within microglia[10]. Notably, this study reveals that GRg1 reduces the number of both microglia and dead/dying neurons within the ischemic penumbra in a CKLF1-dependent manner. A central question is why GRg1

Figure 8 GRg1 promotes microglial degradation *via* the CKLF1/CCR4/mTORC1/TFEB pathway. (A) Experimental design for cargo degradation, TFEB activation, and Western blotting. BV-2 microglia were subjected to OGD/R and co-cultured with apoptotic SH-SY5Y-mCherry cells, which were treated with either GRg1 (10 μmol/L) or rapamycin (100 nmol/L) in the presence or absence of CKLF1-C27 (1 μmol/L) for 3 h. Cells were then washed to remove non-internalized ACs, and real-time fluorescence imaging (0−6 h) was performed using confocal microscopy. The experimental protocols for TFEB activation, qPCR analysis, and Western blotting were consistent with those used for cargo degradation analysis, except that apoptotic cells were derived from SH-SY5Y cells and detection was performed 3 h after rinsing. (B) Representative immunofluorescence images depicting TFEB expression in BV-2 cells. (C) Percentage of cells with TFEB nuclear localization relative to total cells ($n = 4$ random fields; $^{*}P < 0.05$, $^{**}P < 0.01$, $^{***}P < 0.001$; one-way ANOVA followed by Tukey's *post hoc* test). (D) The mRNA levels of TFEB target genes (*Mcoln1*, *Atp6v1h*, *Atp6v0d1*, *Ctsb*, and *Ctsf*) ($n = 4$; $^{*}P < 0.05$, $^{**}P < 0.01$, $^{***}P < 0.001$; one-way ANOVA followed by Tukey's *post hoc* test). (E, F) Phosphorylation levels of mTOR (Ser2448) and TFEB (Ser211) in BV-2 microglia were analyzed ($n = 4$; $^{**}P < 0.01$, $^{***}P < 0.001$; one-way ANOVA followed by Tukey's *post hoc* test). (G, H) Analysis of TFEB nuclear translocation in *Ccr4*-KO BV-2 cells subjected to OGD/R and treated with CKLF1-C27 (1 μmol/L) and/or GRg1 (10 μmol/L) during efferocytosis ($n = 4$ random fields; one-way ANOVA followed by Tukey's *post hoc* test). (I, J) Analysis of TFEB nuclear translocation in BV-2 cells subjected to OGD/R and treated with CKLF1-C27 (1 μmol/L), GRg1 (10 μmol/L), and/or Rapamycin (100 nmol/L) during efferocytosis ($n = 4$ random fields; $^{***}P < 0.001$, one-way ANOVA followed by Tukey's *post hoc* test). (K) Representative images of efferocytosis *Tfeb*-KO BV-2 cells at 0, 3, and 6 h after washout of non-internalized ACs. (L) Quantification of apoptotic SH-SY5Y cargo degradation in efferocytosis *Tfeb*-KO BV-2 cells, AC counts per unit area at 0 h in each group were normalized to 1 ($n = 4$ random fields; $^{**}P < 0.01$; two-way ANOVA, Sidak's multiple comparisons test). (M) Schematic summary: GRg1 binds to CKLF1-C27 to antagonize CCR4 activation, thereby inhibiting mTOR phosphorylation, promoting TFEB activation, and enhancing microglial degradation.

reduces the number of dead/dying neurons while exerting no significant impact on microglial internalization capacity. These phenomena shifted our focus to microglial degradation, where we found that GRg1 significantly enhanced lysosomal activity, a finding corroborated by *in vitro* degradation assays. The inability of GRg1 to inhibit CKLF1-induced enhancement of microglial internalization may be attributed to its elevation of *Il10* and *Tgfb* mRNA levels, which are reported to exert pronounced pro-internalization effects[45,46].

Lysosomes, as organelles responsible for degrading biological macromolecules (including proteins, nucleic acids, and polysaccharides), serve a central role in the degradation of internalized substances by phagocytes[47]. TFEB functions as a master regulator of lysosomal biogenesis and function, with its activation predominantly regulated by protein−protein interactions and post-translational modifications[48,49]. Among these mechanisms, mTORC1 is a well-characterized signaling pathway that phosphorylates TFEB to modulate its activation state[50]. Building on this basis, we investigated the role of GRg1 in rescuing CKLF1-impaired lysosomal function and alleviating impeded microglial degradation during efferocytosis. Our data reveal a novel mechanism underlying the anti-AIS effects of GRg1, which targets CKLF1 to enhance lysosomal function and accelerate microglial degradation through the CCR4/mTORC1/TFEB signaling pathway.

5. Conclusions

This study identifies GRg1 as a natural CKLF1 inhibitor that enhances the clearance of dead/dying neuron *via* the CKLF1/CCR4/mTORC1/TFEB pathway, providing a molecular explanation for the anti-AIS effects of PNS. The integrated screening strategy established herein offers a framework for discovering targeted inhibitors from complex natural products, while the uncovered mechanism advances our understanding of lysosomal regulation in post-ischemic neuroinflammation. GRg1 represents a promising candidate for AIS therapy, with the potential to address the unmet need for anti-neuroinflammatory agents targeting efferocytosis and lysosomal function.

Acknowledgments

This study was supported by the National Natural Science Foundation of China (Nos. U2202214, 82074044, U21A20410, 82374060, and 82130109), the CAMS Innovation Fund for Medical Sciences (No. 2025-I2M-XHXX-099, China), the Central Government Guidance Funds for Local Science and Technology Development Projects of Xinjiang Uygur Autonomous Region (No. ZYYD2026QY05, China), and the China Postdoctoral Science Foundation (No. 2025M783916).

Author contributions

Pinglong Fan: Conceptualization, Methodology, Investigation, Visualization, Funding acquisition, Writing-original draft, Writing-review & editing. Yuan Ruan: Conceptualization, Methodology, Investigation, Visualization, Writing-review & editing. Kaichao Hu: Methodology, Investigation. Hongyun Wang: Investigation. Junrui Ye: Investigation. Shasha Wang: Investigation. Ruolan Yuan: Investigation. Guangyi Yang: Investigation. Fangmin Liu: Investigation. Wenbin He: Investigation. Gang Li: Investigation. Xu Yan: Investigation. Shifeng Chu: Conceptualization, Visualization, Funding acquisition, Writing-original draft, Writing-review & editing. Zhao Zhang: Conceptualization, Visualization, Funding acquisition, Writing-review & editing. Naihong Chen: Conceptualization, Funding acquisition, Project administration.

Conflicts of interest

The authors declare no conflicts of interest.

Data availability

The datasets used and/or analyzed during the current study are available from the corresponding author upon reasonable request.

Appendix A. Supporting information

Supporting information to this article can be found online at https://doi.org/10.1016/j.apsb.2026.04.003.

References

1. Mendelson SJ, Prabhakaran S. Diagnosis and management of transient ischemic attack and acute ischemic stroke: a review. *JAMA* 2021;**325**:1088−98.
2. Xu A, Zhang H, Zhang Y, Wu J, Huang Z. Ischemic stroke and intervention strategies based on the timeline of stroke progression: review and prospects. *Acta Pharm Sin B* 2025;**15**:4543−81.
3. Qin C, Yang S, Chu YH, Zhang H, Pang XW, Chen L, et al. Signaling pathways involved in ischemic stroke: molecular mechanisms and therapeutic interventions. *Signal Transduct Targeted Ther* 2022;**7**:215.
4. Shi K, Tian DC, Li ZG, Ducruet AF, Lawton MT, Shi FD. Global brain inflammation in stroke. *Lancet Neurol* 2019;**18**:1058−66.
5. Doran AC, Yurdagul Jr A, Tabas I. Efferocytosis in health and disease. *Nat Rev Immunol* 2020;**20**:254−67.
6. Mehrotra P, Ravichandran KS. Drugging the efferocytosis process: concepts and opportunities. *Nat Rev Drug Discov* 2022;**21**:601−20.
7. Chen C, Chu SF, Ai QD, Zhang Z, Chen NH. CKLF1/CCR5 axis is involved in neutrophils migration of rats with transient cerebral ischemia. *Int Immunopharmacol* 2020;**85**:106577.
8. Wang HY, Ye JR, Peng Y, Ma WY, Chen HD, Sun HS, et al. CKLF induces microglial activation *via* triggering defective mitophagy and mitochondrial dysfunction. *Autophagy* 2024;**20**:590−613.
9. Zhou X, Zhang YN, Li FF, Zhang Z, Cui LY, He HY, et al. Neuronal chemokine-like-factor 1 (CKLF1) up-regulation promotes M1 polarization of microglia in rat brain after stroke. *Acta Pharmacol Sin* 2022;**43**:1217−30.
10. Fan PL, Lai HQ, Wang HY, Hu KC, Ruan Y, Ye JR, et al. CKLF1 disrupts microglial efferocytosis following acute ischemic stroke by binding to phosphatidylserine. *Cell Death Differ* 2025;**32**:1499−517.
11. Hu KR, Zhou ZH, Li HF, Xiao JJ, Shen Y, Ding K, et al. Regulation of histidine metabolism by *Lactobacillus Reuteri* mediates the pathogenesis and treatment of ischemic stroke. *Acta Pharm Sin B* 2025;**15**:239−55.
12. Liu L, Li J, Wang YL, Gong P, Feng JT, Xiao SL, et al. Effects of *Panax notoginseng* saponins on alleviating low shear induced

endothelial inflammation and thrombosis *via* Piezo1 signalling. *J Ethnopharmacol* 2024;**335**:118639.
13. Li H, Deng CQ, Chen BY, Zhang SP, Liang Y, Luo XG. Total saponins of *Panax notoginseng* modulate the expression of caspases and attenuate apoptosis in rats following focal cerebral ischemia−reperfusion. *J Ethnopharmacol* 2009;**121**:412−8.
14. Shi LG, Sun ZY, Su W, Xu F, Xie D, Zhang QX, et al. Treg cell-derived osteopontin promotes microglia-mediated white matter repair after ischemic stroke. *Immunity* 2021;**54**:1527−42.
15. Peng Y, Ye JR, Wang SS, He WB, Feng ZP, Sun HS, et al. A small molecule 20C from *Gastrodia* elata inhibits α-synuclein aggregation and prevents progression of Parkinson's disease. *Cell Death Dis* 2023;**14**:594.
16. He JQ, Yuan RL, Jiang YT, Peng Y, Ye JR, Wang SS, et al. Esculetin facilitates post-stroke rehabilitation by inhibiting CKLF1-mediated neutrophil infiltration. *Acta Pharmacol Sin* 2025;**46**:52−65.
17. Chen J, Li Y, Wang L, Zhang Z, Lu D, Lu M, et al. Therapeutic benefit of intravenous administration of bone marrow stromal cells after cerebral ischemia in rats. *Stroke* 2001;**32**:1005−11.
18. Yang S, Qin C, Chen M, Chu YH, Tang Y, Zhou LQ, et al. TREM2-IGF1 mediated glucometabolic enhancement underlies microglial neuroprotective properties during ischemic stroke. *Adv Sci (Weinh)* 2024;**11**:e2305614.
19. Ma WY, Wu QL, Wang SS, Wang HY, Ye JR, Sun HS, et al. A breakdown of metabolic reprogramming in microglia induced by CKLF1 exacerbates immune tolerance in ischemic stroke. *J Neuroinflammation* 2023;**20**:97.
20. Barca C, Wiesmann M, Calahorra J, Wachsmuth L, Döring C, Foray C, et al. Impact of hydroxytyrosol on stroke: tracking therapy response on neuroinflammation and cerebrovascular parameters using PET-MR imaging and on functional outcomes. *Theranostics* 2021;**11**:4030−49.
21. Yang L, Li XT, Zhao Y, Chen H, Wang C, Wu AR, et al. NAT10 inhibition alleviates astrocyte autophagy by impeding ac4C acetylation of *Timp1* mRNA in ischemic stroke. *Acta Pharm Sin B* 2025;**15**:2575−92.
22. Beccari S, Sierra-Torre V, Valero J, Pereira-Iglesias M, García-Zaballa M, Soria FN, et al. Microglial phagocytosis dysfunction in stroke is driven by energy depletion and induction of autophagy. *Autophagy* 2023;**19**:1952−81.
23. Liu HB, Lu XY, Hu Y, Fan XH. Chemical constituents of *Panax ginseng* and *Panax notoginseng* explain why they differ in therapeutic efficacy. *Pharmacol Res* 2020;**161**:105263.
24. Fu XZ, Chen K, Li Z, Fan HY, Xu B, Liu M, et al. Pharmacokinetics and oral bioavailability of *Panax Notoginseng* saponins administered to rats using a validated UPLC−MS/MS method. *J Agric Food Chem* 2023;**71**:469−79.
25. Liu JJ, Wang YT, Qiu L, Yu YY, Wang CM. Saponins of *Panax Notoginseng*: chemistry, cellular targets and therapeutic opportunities in cardiovascular diseases. *Expet Opin Invest Drugs* 2014;**23**:523−39.
26. Ai QD, Chen C, Chu SF, Zhang Z, Luo Y, Guan FF, et al. IMM-H004 therapy for permanent focal ischemic cerebral injury *via* CKLF1/CCR4-mediated NLRP3 inflammasome activation. *Transl Res* 2019;**212**:36−53.
27. Liu YY, Liu LJ, Zhou Y, Zhou P, Yan QJ, Chen XB, et al. CKLF1 enhances inflammation-mediated carcinogenesis and prevents doxorubicin-induced apoptosis *via* IL6/STAT3 signaling in HCC. *Clin Cancer Res* 2019;**25**:4141−54.
28. Li G, Li GY, Wang ZZ, Ji HJ, Wang DM, Hu JF, et al. The chemokine-like factor 1 induces asthmatic pathological change by activating nuclear factor-κB signaling pathway. *Int Immunopharmacol* 2014;**20**:81−8.
29. Knab F, Koch SP, Major S, Farr TD, Mueller S, Euskirchen P, et al. Prediction of stroke outcome in mice based on noninvasive MRI and behavioral testing. *Stroke* 2023;**54**:2895−905.
30. Goubran M, Leuze C, Hsueh B, Aswendt M, Ye L, Tian Q, et al. Multimodal image registration and connectivity analysis for integration of connectomic data from microscopy to MRI. *Nat Commun* 2019;**10**:5504.
31. Schroer AB, Ventura PB, Sucharov J, Misra R, Chui MKK, Bieri G, et al. Platelet factors attenuate inflammation and rescue cognition in ageing. *Nature* 2023;**620**:1071−9.
32. Huang Y, Jiang W, Zhou RB. DAMP sensing and sterile inflammation: intracellular, intercellular and inter-organ pathways. *Nat Rev Immunol* 2024;**24**:703−19.
33. Singh K, Roy M, Prajapati P, Lipatova A, Sripada L, Gohel D, et al. NLRX1 regulates TNF-α-induced mitochondria−lysosomal crosstalk to maintain the invasive and metastatic potential of breast cancer cells. *Biochim Biophys Acta Mol Basis Dis* 2019;**1865**:1460−76.
34. Aits S, Kricker J, Liu B, Ellegaard A-M, Hämälistö S, Tvingsholm S, et al. Sensitive detection of lysosomal membrane permeabilization by lysosomal galectin puncta assay. *Autophagy* 2015;**11**:1408−24.
35. Burbidge K, Rademacher DJ, Mattick J, Zack S, Grillini A, Bousset L, et al. LGALS3 (galectin 3) mediates an unconventional secretion of SNCA/α-synuclein in response to lysosomal membrane damage by the autophagic−lysosomal pathway in human midbrain dopamine neurons. *Autophagy* 2022;**18**:1020−48.
36. Wang B, Martini-Stoica H, Qi C, Lu TC, Wang S, Xiong W, et al. TFEB-vacuolar ATPase signaling regulates lysosomal function and microglial activation in tauopathy. *Nat Neurosci* 2024;**27**:48−62.
37. Tan A, Prasad R, Lee C, Jho EH. Past, present, and future perspectives of transcription factor EB (TFEB): mechanisms of regulation and association with disease. *Cell Death Differ* 2022;**29**:1433−49.
38. Dewi FRP, Jiapaer S, Kobayashi A, Hazawa M, Ikliptikawati DK, Hartono A, et al. Nucleoporin TPR (translocated promoter region, nuclear basket protein) upregulation alters MTOR-HSF1 trails and suppresses autophagy induction in ependymoma. *Autophagy* 2021;**17**:1001−12.
39. Marwarha G, Prasanthi JR, Schommer J, Dasari B, Ghribi O. Molecular interplay between leptin, insulin-like growth factor-1, and β-amyloid in organotypic slices from rabbit hippocampus. *Mol Neurodegener* 2011;**6**:41.
40. Endres M, Moro MA, Nolte CH, Dames C, Buckwalter MS, Meisel A. Immune pathways in etiology, acute phase, and chronic sequelae of ischemic stroke. *Circ Res* 2022;**130**:1167−86.
41. Matzinger P. Tolerance, danger, and the extended family. *Annu Rev Immunol* 1994;**12**:991−1045.
42. Alexander SP, Fabbro D, Kelly E, Mathie A, Peters JA, Veale EL, et al. The concise guide to pharmacology 2021/22: catalytic receptors. *Br J Pharmacol* 2021;**178**(Suppl 1):S264−312.
43. Liu YQ, Wu L, Peng WJ, Mao XY. Glial polarization in neurological diseases: molecular mechanisms and therapeutic opportunities. *Ageing Res Rev* 2025;**104**:102638.
44. Wu LF, Song HQ, Zhang C, Wang AX, Zhang BW, Xiong CY, et al. Efficacy and safety of *Panax notoginseng* saponins in the treatment of adults with ischemic stroke in China: a randomized clinical trial. *JAMA Netw Open* 2023;**6**:e2317574.
45. Sukka SR, Ampomah PB, Darville LNF, Ngai D, Wang X, Kuriakose G, et al. Efferocytosis drives a tryptophan metabolism pathway in macrophages to promote tissue resolution. *Nat Metab* 2024;**6**:1736−55.
46. Schilperoort M, Ngai D, Katerelos M, Power DA, Tabas I. PFKFB2-mediated glycolysis promotes lactate-driven continual efferocytosis by macrophages. *Nat Metab* 2023;**5**:431−44.

47. Bonacina F, Zhang X, Manel N, Yvan-Charvet L, Razani B, Norata GD. Lysosomes in the immunometabolic reprogramming of immune cells in atherosclerosis. *Nat Rev Cardiol* 2025;**22**:149−64.
48. Settembre C, Di Malta C, Polito VA, Garcia Arencibia M, Vetrini F, Erdin S, et al. TFEB links autophagy to lysosomal biogenesis. *Science* 2011;**332**:1429−33.
49. Chao XJ, Niu MW, Wang SG, Ma XW, Yang X, Sun H, et al. High-throughput screening of novel TFEB agonists in protecting against acetaminophen-induced liver injury in mice. *Acta Pharm Sin B* 2024; **14**:190−206.
50. Vega-Rubin-de-Celis S, Peña-Llopis S, Konda M, Brugarolas J. Multistep regulation of TFEB by MTORC1. *Autophagy* 2017;**13**:464−72.